



## BIROn - Birkbeck Institutional Research Online

Gezatt, J.N. and Macdonald, D.I.M. and Stephenson, R. and Jelinek, A.R. and Carter, Andrew (2021) South Atlantic passive margin evolution: a thermochronology case study from the Rio de Janeiro-Três Rios section, SE Brazil. *Journal of South American Earth Sciences* 106 (103051), pp. 1-13. ISSN 0895-9811.

Downloaded from: <https://eprints.bbk.ac.uk/id/eprint/41765/>

*Usage Guidelines:*

Please refer to usage guidelines at <https://eprints.bbk.ac.uk/policies.html>

or alternatively

contact [lib-eprints@bbk.ac.uk](mailto:lib-eprints@bbk.ac.uk).

1 **South Atlantic passive margin evolution: a thermochronology case study from the Rio de**  
2 **Janeiro-Três Rios section, SE Brazil**

3

4 J. N. Gezatt\* [1]; D. I. M. Macdonald [1]; R. Stephenson [1]; A. R. Jelinek [2]; A. Carter [3]

5 [1] Department of Geology and Petroleum Geology, University of Aberdeen, King's College,  
6 Aberdeen, AB24 3UE, UK.

7 [2] Departamento de Geodésia, Instituto de Geociências, Universidade Federal do Rio Grande do Sul.  
8 Av. Bento Gonçalves, 9500. Porto Alegre, Rio Grande do Sul, CEP 90650-970, Brazil.

9 [3] Department of Earth and Planetary Sciences, Birkbeck College, Malet Street, London, WC1E  
10 7HX, UK.

11 \*Correspondence (gezatt@abdn.ac.uk)

12

13 **Abstract**

14 The southeastern Brazilian passive margin records a complex post-rift evolution, with two parallel  
15 high-elevation features formed after the opening of the South Atlantic. We applied apatite fission  
16 track (AFT) and U-Th/He (AHe) low temperature thermochronology to constrain the thermo-tectonic  
17 history of the Serra do Mar escarpment in the area of Rio de Janeiro state. New AFT central ages for  
18 basement areas collected from a N-S transect orthogonal to the shoreline between the cities of Rio de  
19 Janeiro and Três Rios, range between  $98.5 \pm 5.3$  and  $54.1 \pm 4.2$  Ma, with mean track lengths between  
20  $12.34 \pm 0.40$  and  $14.63 \pm 0.17$   $\mu\text{m}$ . Uncorrected AHe ages lie between  $68.1 \pm 5.9$  and  $60.2 \pm 7.3$  Ma  
21 and are consistent with AFT results. Inverse thermal history models constrained by AFT and AHe  
22 data imply earliest cooling onset from the Barremian (Early Cretaceous), with steady rates more  
23 common for samples closer to coastal areas. Maximum depths of denudation are between 2.5 and 4.5  
24 km. Published thermochronological data from adjacent areas combined with the new results shows a  
25 seemingly simpler post-rift evolution for the area, although suggesting structural control of age  
26 distribution and exhumation.

27

28 **Keywords:** fission track, (U-Th)/He, passive margin, thermal history modelling, southeastern Brazil,  
29 thermochronology

30

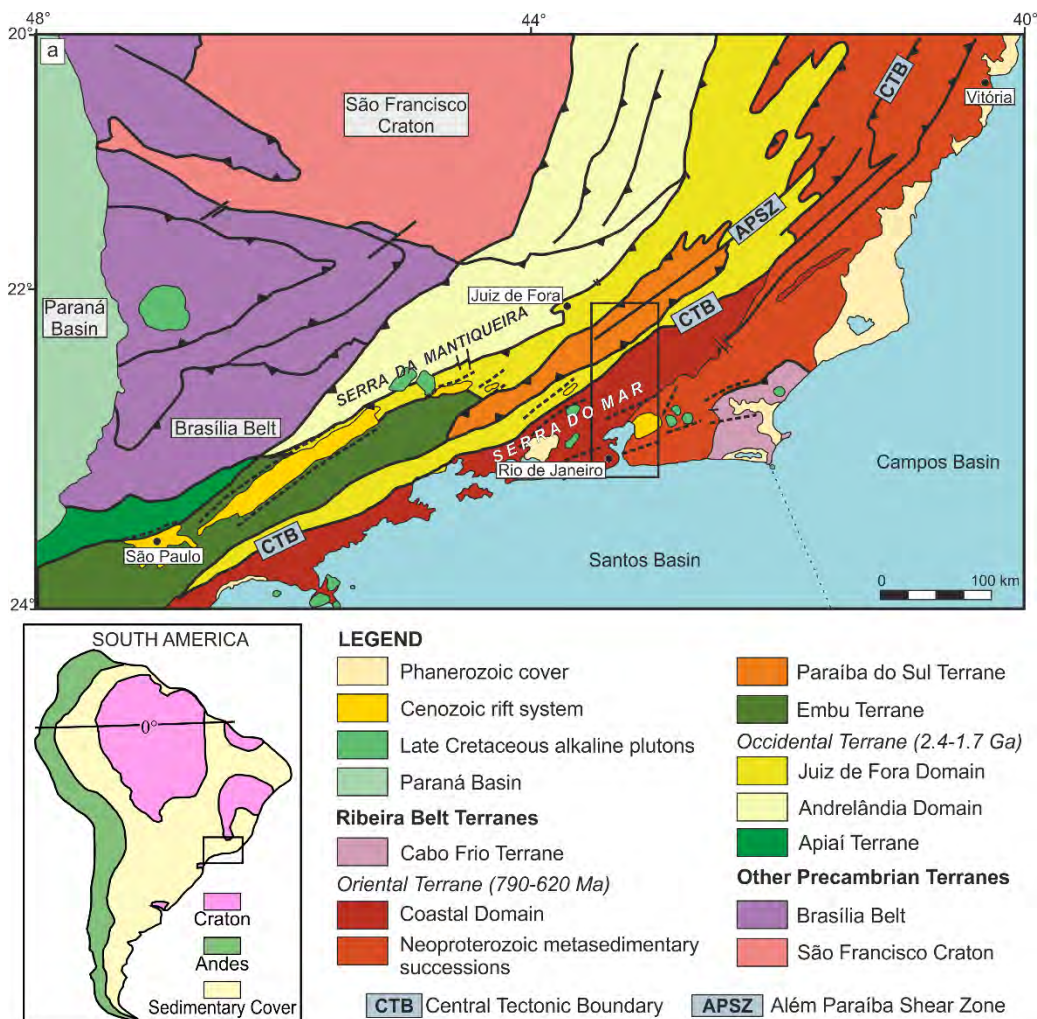
31 **1 Introduction**

32

33 Passive continental margins yield a valuable record of continental rifting as well as of other  
34 lithosphere and mantle dynamic processes. Rifted margin escarpments are significant  
35 geomorphological features that separate elevated regional-scale plateaus from neighbouring low-lying  
36 coastal plains on a number of continental passive margins around the world, known as high-elevation  
37 rifted margins (Gilchrist and Summerfield 1990). There is considerable debate on whether these

38 features were inherited from the rifting process or earlier orogenic events, or if they reflect post-rift  
 39 tectonic reactivation (Gallagher et al. 1994; Brown et al. 2002; Nielsen et al. 2009; Japsen et al. 2012;  
 40 Blenkinsop and Moore 2013; Jelinek et al. 2014).

41 The Atlantic rifted margins represent a particularly complex puzzle, especially given their  
 42 significant geographical extent and assemblage of geological features. The Brazilian passive margin,  
 43 topographically and bathymetrically distinct from its African conjugate (Gallagher and Brown 1997;  
 44 Aslanian et al. 2009), can be divided into at least two segments with distinct rifting responses during  
 45 the Jurassic-Cretaceous opening of the South Atlantic Ocean (Chang et al. 1992; Heine et al. 2013;  
 46 Brune et al. 2018). The Equatorial segment developed in response to transform motion between the  
 47 continental plates, while the remainder of the passive margin, further south, evolved from oblique to  
 48 orthogonal extension. Specifically, the modern coastline in the southeastern segment of the Brazilian  
 49 margin is subparallel to the main NE-SW Precambrian structures, as the propagation of the rift system  
 50 seems to have followed major pre-existing Brasiliano-Pan-African structures (Tommasi and Vauchez,  
 51 2001; Buiter and Torsvik, 2014; Schmitt et al. 2016). Continental breakup in the area took place  
 52 around 130 Ma (Chang et al. 1992; Macdonald et al. 2003). Figure 1 shows the tectonic setting of the  
 53 southeastern segment of the Brazilian continental margin and the location of the present study.



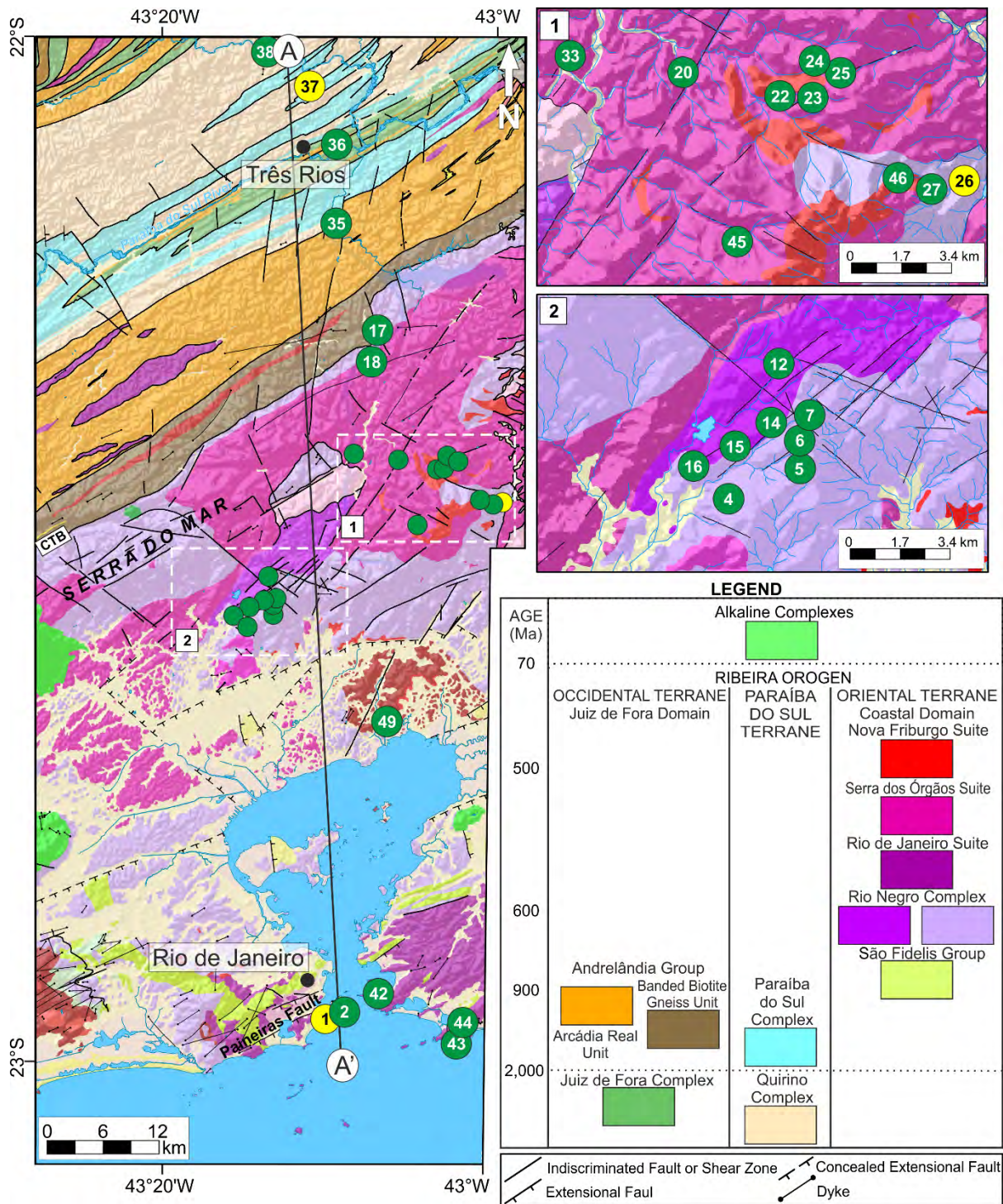
55 **Figure 1.** Geotectonic map of the SE rifted margin in Brazil (after Heilbron et al. 2008). The black  
56 dashed lines outline the Cenozoic rift system onshore structural framework. The black box outlines  
57 the location of the study area of this work. Refer to text for detail on the regional geology.

58

59 The southeastern portion of the Brazilian continental margin contains two escarpments  
60 parallel to the shoreline that reach up to 2000 m above sea level: the Serra da Mantiqueira, farthest  
61 inland, and the Serra do Mar, closer to the coast, separated from the continental shelf onshore of the  
62 marginal Santos Basin by a narrow coastal plain (Figs. 1,2). The study of the present-day regional  
63 landscape can constrain the formation of the high elevation features and help unveil the evolution of  
64 the rifted margin and its contribution to the sedimentary input of the offshore adjacent basins (Karner  
65 and Driscoll 1999; Milani et al. 2001; Macdonald et al. 2003).

66 Low-temperature thermochronology is an ideal tool to investigate upper crust thermal and  
67 erosional histories, as it records the effect of cooling and heating episodes within the shallow crust  
68 that can, in turn, reflect regional geodynamic processes and their surface development. Apatite fission  
69 track analysis (AFT) is sensitive to temperatures between 120 °C and 60 °C (Gleadow et al. 1986;  
70 Wagner et al. 1989; Donelick et al. 2005) and apatite U-Th/He dating (AHe), to temperatures between  
71 ~120°C - 40 °C (Farley, 2000; Flowers et al., 2009; Gautheron et al., 2009; Ault et al., 2019). The  
72 application of these methods can help indicate if the high topography features are remnant of rifting or  
73 if there is thermal record of post-rift tectonic activity (Brown et al. 1990; Gallagher et al. 1994;  
74 O’Sullivan et al. 2000; McGregor et al. 2013; Wildman et al. 2015, 2019).

75 This study provides new regional constraints to the post-rift thermal evolution of the Rio de  
76 Janeiro-Três Rios segment of the SE Brazilian continental margin from AFT and AHe analysis (Fig.  
77 2). Whilst the Brazilian rifted margin has been the subject of previous thermochronological  
78 investigations, there is a data gap in the margin section in the state of Rio de Janeiro and, hence, the  
79 understanding of the rifted margin in the SE of Brazil is incomplete. To address this we collected a  
80 strategic suit of samples across this previously unstudied segment of the continental margin for apatite  
81 thermochronology. The resulting data will help to provide a more complete margin-wide  
82 comprehension of the geodynamic mechanisms responsible for the present-day topography in the  
83 area. We present cooling ages as well as evidence of steady cooling after the breakup of SW  
84 Gondwana and, coupled with previously published regional low-temperature data, point out potential  
85 geological controls for the uplift process that led to the formation of the Serra do Mar escarpment in  
86 the state of Rio de Janeiro, comparing it to other segments of the SE Brazilian continental margin.



87  
88  
89  
90  
91  
92  
93

**Figure 2.** Sample locations in the study area (for location of the geological map see Figure 1). CTB is the Central Tectonic Boundary. Geological map from CPRM (2009a,b). Location of the Paineiras Fault after Ferrari (2001). Samples undergone AFT analysis are labelled in green, while yellow labels indicate those samples analysed with both AFT and AHe methods.

## 94 2 Geological Setting

95

96 The lithologies that occur throughout the present-day SE Brazilian passive margin were  
97 dominantly formed by the Neoproterozoic-Cambrian tectonic events that led to the consolidation of  
98 Western Gondwana during the Brasiliano-Pan-African Orogenic Cycle (Brito Neves and Cordani  
99 1991; Schmitt et al. 2008; Brito Neves et al. 2014). This long-lived convergence event resulted in a  
100 complex NE-SW-striking structural framework formed by high angle strike-slip shear zones (Ebert  
101 and Hasui 1998; Trouw et al. 2000) that comprises syn- to post-orogenic medium- to high-grade  
102 metamorphic rocks and associated magmatic intrusions (Heilbron et al. 2008, 2020). The Ribeira Fold  
103 Belt Precambrian-Cambrian terranes are overlain by the sediments of the Ordovician-Cretaceous  
104 cratonic Paraná Basin to the west (Fig. 1). The Cretaceous volcanic rocks of the Serra Geral  
105 Formation, the Brazilian continental portion of the Paraná-Etendeka Large Igneous Province, have  
106 been dated at  $134.6 \pm 0.6$  Ma by bulk-rock Ar-Ar and zircon/baddeleyite U-Pb (Thiede and  
107 Vasconcelos 2010 and references therein; Janasi et al. 2011, respectively). Unconformably lying on  
108 Late Jurassic rift stage aeolian strata, the flood basalts and acid volcanic rocks were extruded  
109 synchronously with the opening of the South Atlantic and can be correlated to the basement of the  
110 marginal Santos, Campos and Espírito Santos basins (Thomaz Filho et al. 2008; Stica et al. 2014).

111 The marginal Santos and Campos basins started to develop prior to the opening of the South  
112 Atlantic (Chang et al. 1992) and have well known structural frameworks and stratigraphy as a  
113 consequence of extensive surveying for hydrocarbon exploration (e.g. Mohriak et al. 1990; Cainelli  
114 and Mohriak 1999; Modica and Brush 2004; Contreras et al. 2010; Stanton et al. 2010; Beglinger et  
115 al. 2012, Pichel et al. 2019). The main transitional to post breakup source areas of siliciclastic  
116 sediments for these basins have been the Serra do Mar, and later, the Serra da Mantiqueira  
117 escarpments, with sediment transportation and feeding happening mainly through the Paraíba do Sul  
118 River (Cobbold et al. 2001; Zalán and Oliveira 2005).

119 Onshore post breakup magmatism took place between ca. 85 and 55 Ma (Almeida et al. 1996;  
120 Geraldés et al. 2013), emplacing alkaline intrusions such as the Poços de Caldas and Itatiaia  
121 complexes, positioned along what Almeida (1991) named the Cabo Frio Lineament. Thompson et al.  
122 (1998) attributed the alkaline magmatism to the eastward drift of the South American plate over the  
123 Trindade hot spot. Riccomini et al. (2005), on the other hand, argued that radiometric ages of the  
124 alkaline bodies did not show linear progress eastward and that their emplacement was a consequence  
125 of the regional structural framework, where a fracture zone was under influence of a WNW-ESE-  
126 oriented strain.

127 Cenozoic basin formation occurred onshore the Santos Basin after the separation of the Serra  
128 do Mar and Serra da Mantiqueira escarpments as a consequence of structural reactivation (Sacek et al.  
129 2012; Cogné et al. 2013; Franco-Magalhaes et al. 2014; Vieira and Gramani, 2015), during a series of  
130 deformation phases. These processes originated structure-embedded SW-NE to E-W-trending rift

131 basins such as São Paulo, Taubaté, Resende and Guanabara which, among other basins, form the  
132 Cenozoic Continental Rift of Southeast Brazil (Riccomini et al. 2004). Zalán and Oliveira (2005)  
133 identified the offshore associated rifts using gravimetric and magnetic data, and named it the  
134 Cenozoic Rift System of Southeastern Brazil as opposed to a single rift, incorporating the different rift  
135 basins.

136

### 137 **3 Materials and Methods**

138

139 Thirty Precambrian basement outcrop samples were collected in a N-S transect between the  
140 cities of Rio de Janeiro and Três Rios in the Brazilian state of Rio de Janeiro, orthogonal to the  
141 modern shoreline and approximately so to major structural trend. Sampling was generally done on  
142 road cut outcrops observing a desired 100 m vertical distance between sample locations, aiming to  
143 obtain a fairly representative sampling grid of the vertical age distribution along the profile. In total,  
144 49 sites were sampled, while 30 of these had samples analysed by AFT, as the remaining samples  
145 yielded very few or no apatite crystals, or revealed very low uranium concentrations and did not allow  
146 track counting.

147

#### 148 **3.1 Apatite Fission Track**

149

150 Analysis was performed in the London Geochronology Centre at UCL/Birkbeck. Apatite  
151 crystals were separated from ~5-kg samples using standard crushing, sieving, magnetic, and heavy  
152 liquid procedures, and embedded in epoxy resin for fission track analysis. The polished grains were  
153 then treated with 5.0 M HNO<sub>3</sub> for 20 seconds at 21 °C to reveal spontaneous tracks (Hurford 1990).  
154 Following attachment of a low-U mica external detector (Gleadow 1981; Hurford and Green 1982),  
155 Durango and Fish Canyon Tuff apatite standards, and CN5 dosimeter glasses, samples were irradiated  
156 in the Forschungsneutronenquelle Heinz Maier–Leibnitz (FRM II) reactor at Technical University of  
157 Munich. Induced tracks in the mica detectors were etched with 48% HF during 18 min at 20 °C.

158 Spontaneous track count was done for 20 grains per sample (when available) using a zeta ( $\zeta$ )  
159 calibration (Hurford 1990) value of  $338.5 \pm 5.0$  for CN5 dosimeter. Samples were counted using a  
160 Zeiss Axioplan microscope with total magnification of 1250x. For confined track and etch pit  
161 diameter (Dpar) measurements (Donelick et al. 2005) a coupled Kinetek XY stage and digitalising  
162 tablet was used under computer control. Confined track lengths were measured for 100 tracks  
163 depending on abundance. Chlorine wt% was done for 15 of the samples and measured using a  
164 Microscan MK5 electron microprobe with a 5 $\mu$ m beam at an acceleration voltage of 15 keV and 6.0  
165 nA current at the University of Aberdeen. AFT results are reported as central ages (Galbraith 1992)  
166 and uncertainties are for 1 $\sigma$  standard error.

167

## 168 3.2 Apatite U-Th/He

169

170 Given that the AFT age data were closely similar, AHe analyses were obtained from 3  
171 samples that represented the sample location, elevation and AFT age range. As the results recorded  
172 effectively the same thermal histories no further AHe analyses were required. Analysis was performed  
173 in the London Geochronology Centre at UCL/Birkbeck. Four to six euhedral inclusion- and fracture-  
174 free grains were analysed per sample. Grains were hand-picked using a binocular microscope and  
175 selected grains further assessed under higher magnification using a Zeiss Axioplan microscope at a  
176 magnification of 1250x. Individual grains packed into a platinum tube were heated with an 808 nm  
177 iodine laser beam to 900-1000°C for 60 seconds, in order to degas the crystal for  $^4\text{He}$  measurement  
178 using a Pfeiffer Prisma 100 with Quadstar QS422 software. Gas volumes were determined by isotope  
179 dilution using two 5800 cc vacuum tanks with gas pipettes for delivering known aliquots of helium.  
180 The  $^4\text{He}$  Standard Tank (Q Tank), pipette volume 0.3222 cc contains isotopically pure  $^4\text{He}$  that is used  
181 as the gas standard against which samples and blanks are determined. The  $^3\text{He}$  Spike Tank, pipette  
182 volume 0.2258 cc contains isotopically pure  $^3\text{He}$  and is used for isotope dilution of samples and  
183 blanks.

184 Following extraction, the Pt tubes were removed and placed in vials for dissolution. Tube ends  
185 were prised open to ensure solutions could get into the tube and dissolve the apatite grain. A 30 $\mu\text{l}$  spike  
186 with a known concentration of  $^{235}\text{U}$ ,  $^{230}\text{Th}$  and  $^{149}\text{Sm}$ , which included  $\text{HNO}_3$ , was added to each vial and  
187 left for 24 hours at room temperature, enough to dissolve apatite grains. After this, vials were topped  
188 up with 1500  $\mu\text{l}$  of water ready for measurement on an Agilent 7700x ICP-MS. Each solution run  
189 included spike, acid and water blanks plus Durango age standards. Spike solutions were re-calibrated  
190 for each session. Errors on ages use the reproducibility of the Durango age standard which at the time  
191 of analysis was 7%.

192

## 193 3.3 Inverse Thermal Modelling

194

195 Apatite thermal history models were done with software QTQt (Gallagher 2012) which uses a  
196 transdimensional Markov Chain Monte Carlo (MCMC) inversion to sample from possible thermal  
197 histories (Gallagher 1995) and build a spectrum of models which probabilistically fit the thermal data  
198 input. Modelling was carried out for 22 samples with more than 50 confined track length  
199 measurements using multi-kinetic annealing model from Ketcham et al. (2007) and using track  
200 lengths projected against their orientation to the crystallographic c-axis. Samples with AHe analysis  
201 were modelled using the Flowers et al. (2009) radiation damage model with spherical geometry  
202 diffusion. The model choice was based on the protracted cooling obtained during exploratory runs as  
203 well as on the time of residency in the He partial retention zone (HePRZ). Input data contained



204 individual sample track density counts, composition values (Dpar measurements or Cl wt% when  
205 available), confined track measurements and respective angle to c-axis, and zeta parameter value. In  
206 the absence of geological constraints, forward models were used to test various scenarios such as  
207 samples being at or close to the surface and then reburied, or simple exhumation from depth. As these  
208 runs also defined the oldest tracks (approximate point at which the AFT data cannot constrain older  
209 thermal histories), it was decided to use a t-T constraint of  $130 \pm 10$  Ma and  $120 \pm 10$  °C,  
210 corresponding to the South Atlantic rifting. Surface temperature was set at  $20 \pm 10$  °C.  
211 Models were run for 500 thousand iterations and are reproduced here as an expected curve (the mean  
212 thermal history curve weighted for its posterior probability) with 95% associated credible intervals.  
213 Samples JG-01, JG-26 and RJ-37 were modelled with both AFT and AHe data.

214

## 215 **4 Results**

216

### 217 **4.1 Apatite Fission Track Data**

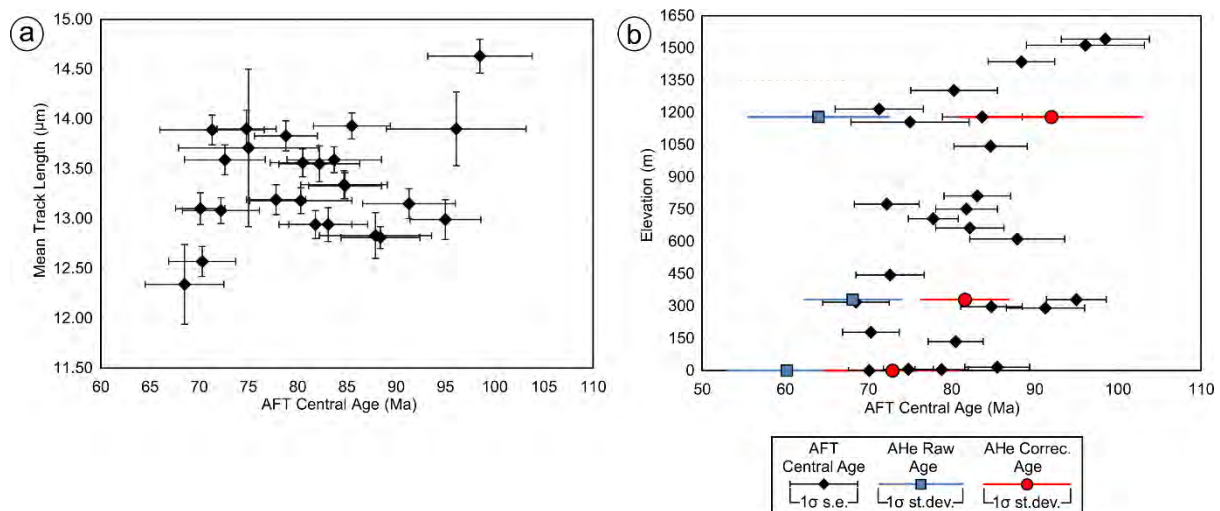
218

219 AFT central ages range between  $98.5 \pm 5.3$  and  $54.1 \pm 4.2$  Ma, with sampling heights lying  
220 between 0 and 1541 meters above sea level (Table 1). Younger ages are found towards the coast, and  
221 become progressively older towards the continental interior, with older ages also found at higher  
222 elevations (Fig. 3). Measured mean confined track lengths (MTL) vary between 12.34 and 13.89  $\mu\text{m}$ ,  
223 while c-axis corrected MTL range between 13.51 and 15.21  $\mu\text{m}$ , and distributions are predominantly  
224 unimodal. Mean Dpar values range from 1.52 to 4.10  $\mu\text{m}$ , illustrating compositional variation between  
225 samples. Sample J-49 has the highest mean Dpar value, the second highest being sample J-45, with  
226 3.60  $\mu\text{m}$ . The highest obtained Cl wt% value 0.06 was for sample JG-16. Sample JG-17, though with  
227 relatively high mean Dpar (3.59  $\mu\text{m}$ ), has very low mean Cl wt% (0.017).

228 Single apatite grains show ages with no statistically significant dispersion and all samples  
229 passed the  $\chi^2$  test, with unimodal single grain age distributions, with the exception of RJ-36, which  
230 has  $P\chi^2$  of 0.6. AFT radial plots and confined track length distributions are presented in the  
231 Supplementary Material.

232

233



234  
235

236 **Figure 3.** AFT age distribution. (a) Relationship between AFT central ages and measured MTL –  
237 boomerang plot (Green 1986; Gallagher and Brown 1997). A trend of post-rift cooling starts around  
238 100 Ma, while a possible second cooling trend could start around 70 Ma; (b) Plot of AFT and AHe  
239 ages against elevation. No clear linear trend can be observed before elevations of 1,200 m.

240

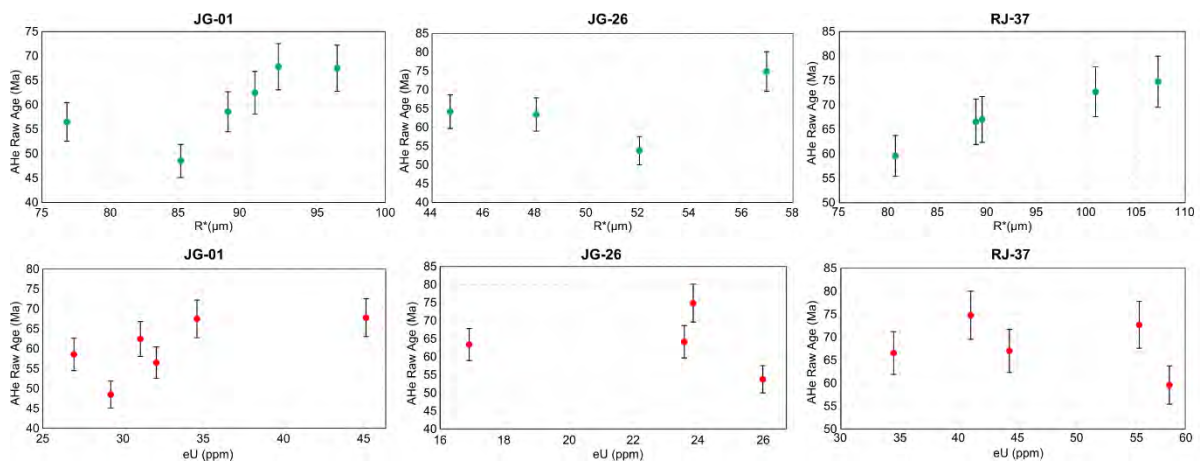
#### 241 4.2 Apatite U-Th/He Data

242

243 Mean  $F_T$ -corrected ages (Farley et al. 1996) vary between  $92.0 \pm 11$  and  $72.9 \pm 8.2$  Ma and  
244 mean AHe raw ages range from  $68.1 \pm 5.9$  to  $60.2 \pm 7.3$  Ma (Table 2). While six single grains were  
245 analysed per sample, two grains in sample JG-26 were excluded due to over-dispersed ages. Similarly,  
246 grain 3 in sample RJ-37 could not be dated since it was lost from its platinum tube. Single-crystal ages  
247 vary between  $74.9 \pm 5.2$  and  $48.5 \pm 3.4$  Ma. All samples show uncorrected ages younger than  
248 corresponding AFT ages. Corrected ages are, in turn, younger than their respective AFT ages, with the  
249 exception of sample JG-26. However, AFT and AHe corrected age for this sample are within error  
250 level of each other.

251 Although the AHe dataset does not yield significant age dispersion ( $>20\%$   $1\sigma$  standard  
252 deviation, Flowers and Kelley, 2011), within-sample age dispersion can be real and contain useful  
253 thermal history information whereby age variation is due to variation in grain size (Farley, 2000;  
254 Stockli et al., 2000; Reiners and Farley, 2001), composition (Gautheron et al., 2013) and/or radiation  
255 damage (Fitzgerald et al. 2006; Shuster et al. 2006; Recanati et al., 2017) as a function of the  $^4\text{He}$   
256 production during a given thermal history. Alternatively, it might be caused by analytical factors such  
257 as unrecognized U-Th-rich inclusion (Lippolt et al., 1994; Farley, 2002), U and Th zonation (Farley,  
258 2002; Meesters and Dunai, 2002a, 2002b; Hourigan et al., 2005; Ault and Flowers, 2012),  
259 implantation from U-Th-rich neighbours (Spiegel et al. 2009; Murray et al. 2014), or the analysis of

260 crystal fragments (Brown et al. 2013). The last was avoided by selecting whole grains. For sample JG-  
 261 26 in particular, there is a weak positive correlation between age and spherical equivalent radius (Fig.  
 262 4), which could be a factor indicating  $F_T$  overcorrection. Furthermore, thorough grain selection  
 263 procedures should have reduced the effect of grain zonation and inclusion, while implantation from  
 264 neighbouring minerals cannot be ruled out. Radiation damage can be assessed through the variation in  
 265 effective uranium (eU, calculated as  $[U] + 0.235[Th]$ , Gastil et al. 1967), for which sample JG-26  
 266 shows a weak negative correlation with AHe age (Fig. 4), whereas a positive correlation implies  
 267 radiation damage for sample JG-01. In general, crystal size is varied with spherical equivalent radius  
 268 ( $R^*$ ) between 44.7 and 107.25 $\mu\text{m}$ , and eU values lie between 16.9 and 57.8 ppm. Samples lack  
 269 significant correlation between  $R^*$  or eU and the AHe ages, with the exception of RJ-37, which shows  
 270 strong positive age- $R^*$  correlation (Fig. 4). The AHe data can be further assessed with inverse thermal  
 271 history models by pairing with the AFT data.  
 272



273  
 274  
 275 **Figure 4.** Plots showing the relationship between single-crystal AHe age and spherical equivalent  
 276 radius ( $R^*$ ), and effective Uranium (eU), respectively. AHe ages are single grain ages uncorrected for  
 277  $\alpha$ -ejection.

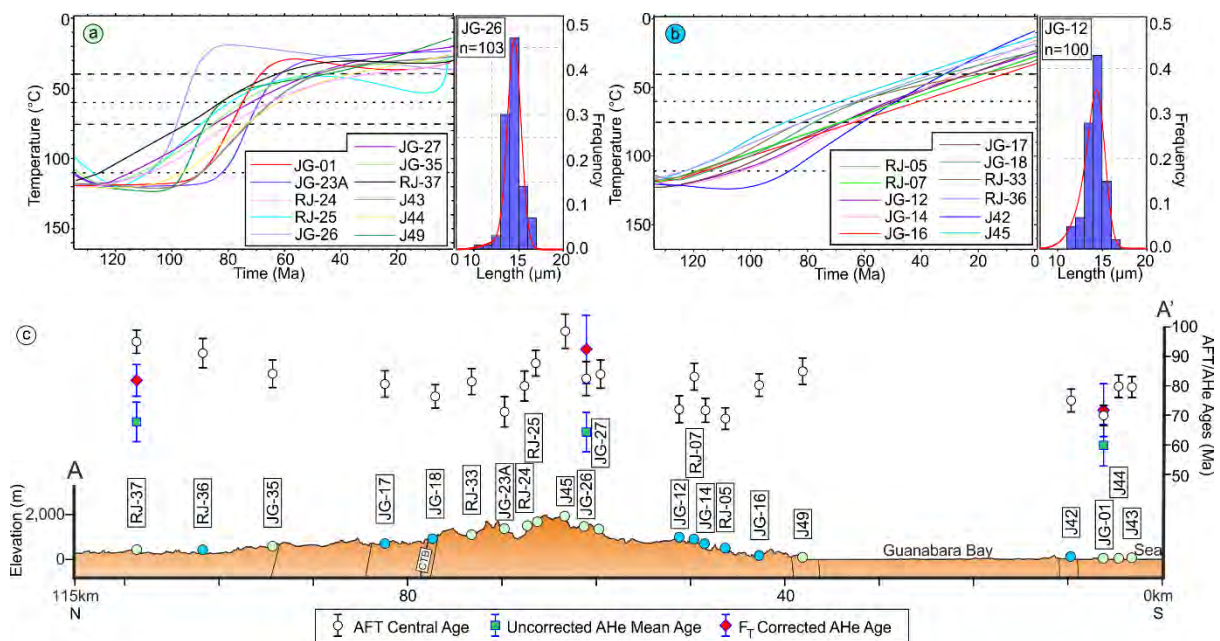
278  
 279 **4.3 Inverse Thermal Modelling**

280  
 281 In general, thermal history models show simple, steady cooling trajectories for samples  
 282 located towards the coast. On the other hand, more complex cooling histories can be seen in areas  
 283 sampled on the escarpment area or further towards the continental interior. There is not, however, a  
 284 clear distribution trend between ‘simple’ and ‘complex’ models regarding proximity to the coast (Fig.  
 285 5). Time-temperature paths shown here are the expected models, which are the mean thermal history  
 286 model weighed for its posterior probability. Complete models for all samples are available in the  
 287 Supplementary Material.

288 The steady cooling models show an onset of cooling mostly between 120 and 100 Ma with an  
 289 average cooling rate of 0.95 °C/Ma, whereas for the complex models the onset of cooling ranges  
 290 between 125 and 80 Ma. The latter bear higher cooling rates during the Late Cretaceous (the highest  
 291 for sample JG-26, 3.6 °C/Ma) followed by a decrease in the cooling rate chiefly between 70 and 50  
 292 Ma, with an average cooling rate of 0.34 °C/Ma before reaching surface temperatures. Samples JG-  
 293 01, RJ-25, JG-26, and RJ-37 show a slight reheating trend then, before reaching surface temperatures.  
 294 However, temperature increase takes place outside of either AFT PAZ and AHe PRZ (for samples  
 295 modelled with AHe data - JG-01, JG-26, and RJ-37) and are, as such, poorly resolved.

296 Estimations of magnitudes of denudation for the modelled samples were calculated as a ratio  
 297 between the cooling trend temperature variation and the geothermal gradient (Raab et al. 2002),  
 298 assumed constant at 25 °C/km. This refers to the regionally-averaged mean value of the thermal  
 299 gradients calculated different sectors of the upper crust in the study area (Hamza et al. 2005a,b; Lima  
 300 Gomes and Hamza, 2005). Total magnitudes of denudation for that thermal gradient range between  
 301 4.5 and 2.5 km. For the regional thermal gradient interval (20-30 °C/km) denudation values range  
 302 between 5.65-3.15 and 3.77-2.1 km, respectively. Younger AFT ages, towards the coast, reflect high  
 303 of erosion rates of the South Atlantic Rift flank, and the more complex thermal history models for  
 304 samples relate to lower magnitudes of denudation towards the continental interior.

305  
 306



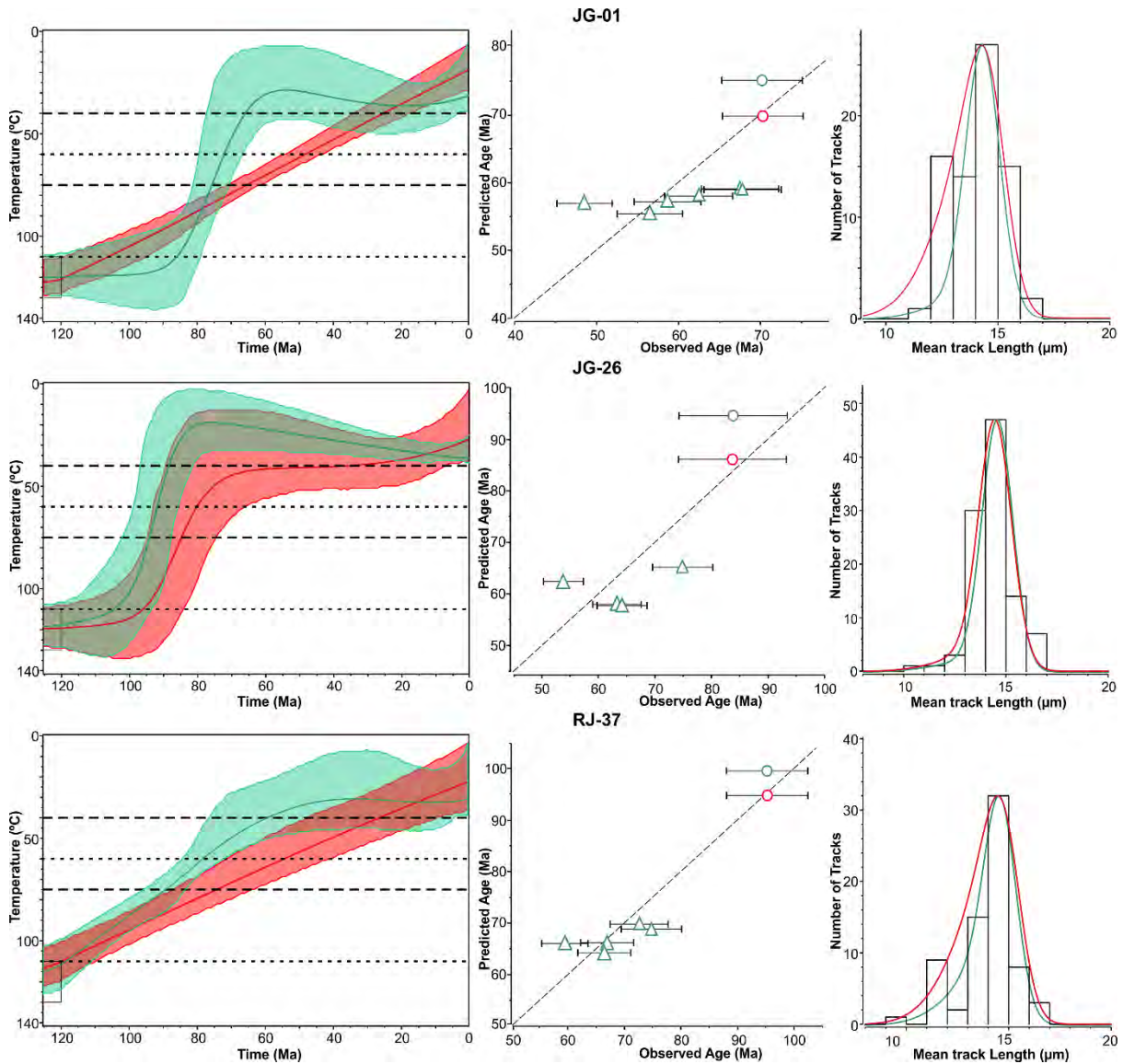
307  
 308  
 309 **Figure 5.** Expected cooling trajectories for modelled samples with representative track length  
 310 distributions. Models are divided into (a) complex models, mostly found towards the continental  
 311 interior and (b) simple models, mostly found for samples closer to the coast, as represented on (c)  
 312 showing representative topographic profiles with modelled sample locations coloured in reference to

313 model trajectory (green for complex models and blue for simple models) with respective AFT and  
314 AHe ages. Schematic main structure position and profile location as shown in Figure 2. Structure  
315 attitude as in Heilbron et al. (2008) and CPRM (2009a,b). CTB is the Central Tectonic Boundary.  
316 Thin dashed lines indicate upper and lower limits of apatite FT partial annealing zone (PAZ), while  
317 long dash lines indicate those of HePRZ for Durango standard kinetics.

318

319 Figure 6 shows thermal history models obtained for samples JG-01, JG-26 and RJ-37,  
320 comparing cooling trajectories modelled with AFT data to those modelled with both AFT and AHe  
321 data. AFT model for sample JG-26 infers rapid cooling in the Early Cretaceous, followed by a  
322 protracted cooling trajectory from the ca. 75 Ma, and a new cooling trend around 20 Ma. The AFT  
323 and AHe model, however, presents an earlier onset of cooling and a higher cooling rate, with mild  
324 reheating after ca. 90 Ma. Models for samples JG-01 and RJ-37, on the other hand, show considerable  
325 change between the cooling curves, from a monotonic cooling trajectory for AFT data alone, to  
326 accelerated Early Cretaceous cooling and slower exhumation around 60 Ma. For all AHe thermal  
327 history models the expected cooling curve remains in temperatures below the resolution of the method  
328 (around 30 °C), while the 95% credible interval is within the upper section of the PRZ during the final  
329 cooling phase in samples JG-01 and RJ-37. For all AHe + AFT models the main inferred cooling  
330 phase takes place during the Cretaceous, with a later onset of cooling for sample JG-01, on the  
331 modern shoreline.

332



333

334

335 **Figure 6.** Cooling history models obtained for coupled AFT and AHe data. For sample thermal  
 336 history models, on the left, central solid line is the expected model with 95% credible interval. Thin  
 337 dashed lines indicate upper and lower limits of AFT Partial Annealing Zone (PAZ), and long dash  
 338 lines indicate those of AHe Partial Retention Zone (PRZ). Central graphs show model age predictions  
 339 versus observed (measured) ages. Green symbols are for combined AFT and AHe models, while red  
 340 symbols are for AFT models. Triangles are for AHe ages, and circles are for AFT central ages. Right  
 341 side graphs present c-axis-projected confined track length distributions for those samples with  
 342 expected prediction models for each thermal model in its respective colour.

343

## 344 5 Discussion

345

### 346 5.1 Cooling history

347

348 Age data and thermal history models indicate a main cooling phase during the Late  
349 Cretaceous from temperatures higher than the apatite closing temperatures, with no pre-rift thermal  
350 age records for the Precambrian basement. As all samples yield post-rift ages, they were interpreted as  
351 cooling ages that reflect basement exhumation from depth. The relationship between AFT ages and  
352 MTL shows a clear post-rift cooling event, while a second trend could suggest a new one around 70  
353 Ma, possibly as a consequence of post-rift tectonic activity (Fig.3a). There is no clear linear  
354 relationship between AFT ages and elevation other than for samples above 1,200 m.a.s.l., where ages  
355 clearly increase with higher altitude (Fig.3b). Although the onset of exhumation is not constrained by  
356 the data, cooling in the Early Cretaceous is likely to have occurred as a response to syn- to post-rift  
357 unloading due to denudation. The rapid initial cooling inferred by some of the complex models is  
358 mostly seen in the samples currently at high elevations or very close to the coast (e.g. JG-01, J44, RJ-  
359 25, JG-26). Accordingly, most of those samples, collected at high-relief locations, yield relatively  
360 older ages, narrower track length distributions and longer mean track lengths. While those samples  
361 yield older central ages, samples RJ-36 and RJ-37, further inland, show AFT central ages of  $91.3 \pm$   
362  $4.7$  and  $95 \pm 3.6$  Ma, respectively, at considerably lower elevations. For that group of samples (Fig.  
363 5a) cooling becomes slower during the Late Cretaceous with significantly lower exhumation rates,  
364 implying that most of them have resided at near-surface temperatures since then. Samples JG-01 and  
365 RJ-25 indicate a third cooling phase in the Neogene, which is not well constrained since cooling  
366 trends are outside the limit of resolution for both AFT (for RJ-25) and AHe (for JG-01). Conversely,  
367 the other thermal model group (Fig. 5b) presents a single cooling trend since the Early Cretaceous.  
368 Groups of samples with similar cooling trajectories (green and blue sample groups for “complex” (a)  
369 and “simple” (b) models, respectively, on the topographic profile in Fig. 5) also seem to have a  
370 contiguous distribution along certain stretches of the transect, suggesting that localised similar thermal  
371 evolutions are a reflection of distinct fault-bounded blocks throughout the transect. For example, the  
372 15-km profile segment on the escarpment with complex thermal models (green) would be a different  
373 block from the 10-km segment with simple cooling trajectories (blue). Those blocks would also be  
374 limited by a less discernible structural framework (and not only the main structures presented in  
375 Figure 5), which is less evident with the observation of the thermal age data alone.

376 Total magnitudes of denudation derived for the area are compatible with estimates from other  
377 studies (Gallagher et al. 1994; Cogné et al. 2011, 2012; Hiruma et al. 2010; Engelmann de Oliveira et  
378 al. 2016) for adjacent areas in the SE margin, between ~2 and 4 km, with higher rates of exhumation  
379 found for areas closer to the coast. Those values are consistent with sediment thicknesses observed for  
380 Late Cretaceous - Paleogene clastic deposits of the proximal Santos and Juréia formations in the  
381 Santos Basin, possibly with important contribution to sand-rich turbiditic deposits in more distal  
382 portions of the basins (Zalán and Oliveira, 2005; Assine et al. 2008). A constant geothermal gradient  
383 of 25 °C/km is assumed over geological time in the absence of paleogeothermal data, although it is  
384 likely that gradients would be higher during and soon after rifting. Early rapid cooling inferred for

385 complex thermal history models and consequent localised higher denudation rates are also consistent  
386 with high rates of sediment supply and basin subsidence observed for the Santos Basin by Contreras  
387 et al. (2010). In contrast, Campanian-Maastrichtian decrease in denudation rates for those sites, more  
388 common on the escarpment area, coincides with reduction in the sedimentation rate (Cobbold et al.  
389 2001; Contreras et al. 2010).

390

## 391 **5.2 Margin Evolution**

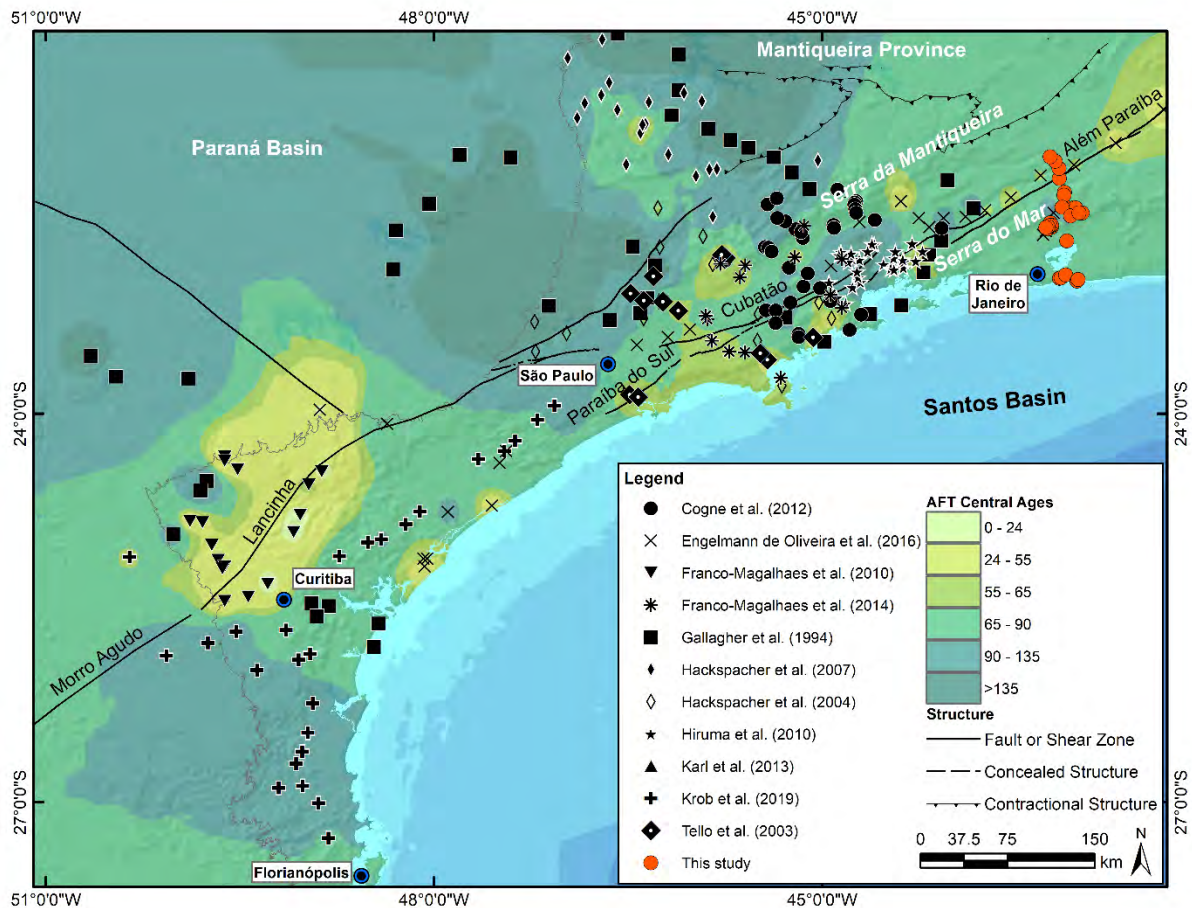
392

393 Thermochronological studies carried out on the southeastern Brazilian continental margin  
394 have estimated significant denudation after breakup, between 2.5 and 4 km. Generally, fission-track  
395 ages become older towards the interior of the continental margin while younger ages (and respective  
396 greater depths of denudation) occur towards the coast. The distinct thermal age ranges found by the  
397 authors have been attributed to cooling phases resulting from different phenomena, from studies often  
398 combining thermochronological dating to additional radiometric methods. Gallagher et al. (1994), in  
399 the most comprehensive regional study regarding the post-rift thermal evolution of the SE continental  
400 margin in Brazil to date, noticed denudation and exhumation did not occur at constant rates  
401 throughout the margin, as higher average rates were seen towards the coast, with more than 3 km of  
402 post-breakup total magnitudes of denudation. The authors found higher complexity in northern and  
403 central regions, likely due to structural reactivation. Hackspacher et al. (2004, 2007) suggested  
404 tectonic uplift and isostatic movement followed by regional erosive processes as a major mechanism  
405 for post-rift thermal events. Hiruma et al. (2010) proposed distinct cooling histories locally controlled  
406 by fault-bounded blocks in the Bocaina Plateau. Similarly, Karl et al. (2013) and Krob et al. (2019)  
407 constrained different crustal blocks for the southeastern and southern segments of the continental  
408 margin with different exhumation and cooling histories in multi-thermochronometer studies,  
409 recognizing fault-bounded block cooling age control by the Neoproterozoic NE-SW structures as well  
410 as by the Atlantic rift transfer zones. Cogné et al. (2011, 2012) and Tello et al. (2003, 2005) described  
411 a Neogene uplift in the Serra da Mantiqueira and Serra do Mar escarpments in the state of São Paulo  
412 within otherwise distinct thermal history trajectories, which was also identified by Engelmann de  
413 Oliveira et al. (2016) for samples in the Paraná Basin and on the Além Paraíba Shear Zone, and  
414 attributed its post-rift localized rapid uplift to plate-wide E-W compressional tectonism and structural  
415 reactivation as a consequence of Late Cretaceous South America western margin collisions. Franco-  
416 Magalhaes et al. (2010) found Late-Cretaceous reactivation of the upper crust, with the youngest AFT  
417 ages in the region, reflecting the intrusion of the Ponta Grossa dyke swarm. The thermal history  
418 models of samples in this study do not have the resolution to confirm changes in cooling rate in the  
419 Neogene.

420 Gallagher et al. (1994) mention considerable age increase for the AFT ages within 50 km of  
421 the present-day coastline. In the present study, however, even though the occurrence of relatively



422 older ages increases towards the continent interior, the age difference is not as pronounced, with the  
 423 total AFT central age amplitude of the data set of  $44.4 \pm 5.3$  Ma. For example, sample JG-38,  
 424 collected the farthest inland, has a central age of  $68.1 \pm 5.1$  Ma, some 110 km from the coast. In that  
 425 sense, the AFT age variability in the area is much lower in compared to other studies in neighbouring  
 426 areas (Fig. 7).



427  
 428 **Figure 7.** Location and AFT central age distribution studies throughout the SE segment of the  
 429 Brazilian continental margin. Younger ages occur towards the coast and in the proximity of large  
 430 geological structures, implying localised reactivation, whereas older ages are common towards the  
 431 continental interior and at high elevation features. Central age isolines were plotted using the  
 432 weighted distance average interpolation tool in software ArcGis 10.5 (ESRI, 2016).

433  
 434 Engelmann de Oliveira et al. (2016) found similar AFT ages and thermal history models for a  
 435 basement sample dataset in Rio de Janeiro near this study area. Samples TR7RJ5, TR7RJ6 and  
 436 TR7RJ7 show cooling ages compatible with those in this study, with AFT central ages ranging  
 437 between  $101.8 \pm 6.6$  and  $73.1 \pm 5.5$  Ma. The remaining ones, modelled together, exhibit a single,  
 438 steady cooling trajectory, much like the cooling histories found for the simpler models in the present  
 439 dataset. Different samples collected along the Além Paraíba Shear Zone on the northern coast, which  
 440 overlaps the northernmost portion of this study area (Fig. 7), yield younger AFT central ages (between

441  $67.5 \pm 5.2$  and  $48.0 \pm 2.9$  Ma) and show a steep cooling trend around 4 Ma, which could suggest  
442 younger relative structural movement. Sample RJ-35, within 1.5-km distance of the shear zone,  
443 doesn't show record of such process, much like sample RJ-36, which seems to be in line with  
444 Engelmann de Oliveira et al. (2016)'s samples TR11RJ3 and TR11RJ4.

445 Post-breakup monotonic cooling is reported for other areas in the SE margin with AFT data  
446 models (Cogné et al. 2011; Engelmann de Oliveira et al. 2016), although often for a single sample  
447 location or a restricted sector. Likewise, the distribution of steady-cooling models in the study area  
448 occurs in segments of the transect, similar to the regional pattern.

449 Cobbold et al. (2001), Riccomini et al. (2004), and Cogné et al. (2012, 2013) found structural  
450 evidence of deformation in the Cenozoic Rift System while evidence of post-rift onshore crustal  
451 reactivation was observed in the thermal data for the SE margin, especially in the Paraíba do Sul  
452 River Valley (Tello et al. 2003, 2005; Cogné et al. 2011, 2012; Franco-Magalhaes et al. 2014;  
453 Engelmann de Oliveira et al. 2016). In the Rio de Janeiro area Ferrari (2001) describes a Campanian -  
454 early Eocene E-W transcurrent event responsible for the reactivation of Ribeira Belt structures and  
455 formation of the Guanabara Graben (Zalán and Oliveira, 2005). Silicified tectonic breccias in fault  
456 zones formed from hydrothermal activity attributed to late-stage alkaline magmatism in the  
457 Guanabara Graben have an alkali-feldspar K-Ar age of  $50.7 \pm 1.2$  Ma (Santos, 1994). The youngest  
458 AFT age in this study is for sample JG-02 of  $54.1 \pm 4.2$  Ma and was collected from one of the areas  
459 where Ferrari (2001) analysed the silicified breccia on the Paineiras Fault (Fig. 2) in the southern area  
460 of the city of Rio de Janeiro, on the coast, where the author observed geometric relationships  
461 indicating that ENE-WSW reactivation was concomitant with hydrothermal activity. The younger  
462 AFT age for sample JG-02 could be related to the reactivation of these structures. Hackspacher et al.  
463 (2004) found similar ages in the coastal area in the state of São Paulo ( $58 \pm 4$  Ma), which the authors  
464 interpreted as an age of reactivation of the Serra do Mar in the area.

465 The present dataset further illustrates the complexity of the post-rift evolution of the Brazilian  
466 continental margin, as numerous factors play different parts in the evolution of distinct segments of  
467 the margin. Karl et al. (2013) and Krob et al. (2019) recognized different blocks in the southern SE  
468 rifted margin with distinct thermal evolutions since the Brasiliano-Pan-African orogenic cycle, bound  
469 by onshore segments of transfer zones. Such sectorisation is likely to be present throughout the  
470 margin, controlled by lithospheric heterogeneity and discontinuities (Meisling et al. 2001; Gallagher  
471 et al. 1994; Wildman et al. 2019; Hueck et al. 2019). Even though regional high-elevation features  
472 share a common post-breakup origin, different segments of the SE margin evolved in a distinct  
473 fashion, influenced by particular combinations of mechanisms, as illustrated by the variability  
474 amongst available thermochronological datasets. In that sense, we present an indication that the Rio  
475 de Janeiro section of the southeastern Brazilian continental margin could have behaved as a distinct  
476 block. The sampled area presents relatively uniform exhumation, behaving in a moderately stable

477 manner throughout the post-breakup evolution of the crustal block, in contrast with the more complex  
478 trends seen in neighbouring areas.

479

## 480 **6. Conclusions**

481

482 New AFT and AHe thermal data for the state of Rio de Janeiro provide new constraints on the  
483 post-breakup evolution of the southeastern segment of the Brazilian continental margin, while  
484 highlighting the diversity of processes responsible for the formation of present-day landscape. Sample  
485 thermal histories record continuous cooling from as early as the Barremian, associated with rift flank  
486 uplift and denudation. Maximum denudation since then is between 2.5 and 4.5 km with greater depths  
487 of erosion occurring towards the coastal area. Such volumes are compatible with the high sediment  
488 input recorded for the offshore basins, while the Campanian-Maastrichtian decrease in cooling rates  
489 observed for samples with more complex cooling histories matches a period of lower sedimentary  
490 budget. The relatively uniform distribution of apatite ages across the study area yields little significant  
491 variation between high and low elevation areas, in contrast with studied adjacent areas that show more  
492 complexity. This contrast points to an important control of the inherited structural framework over the  
493 post-breakup evolution of the rifted margin, as corroborated by other thermochronological studies.

494

## 495 **Acknowledgements**

496

497 We gratefully acknowledge support from Shell Brazil through the BG05: UoA-UFRGS-SWB  
498 Sedimentary Systems project at the University of Aberdeen and UFRGS, and the strategic importance  
499 of the support given by ANP through the RandD levy regulation. CNPq process number  
500 237726/2012-2 for funding under regime GDE of the Science Without Borders Programme. We  
501 would also like to thank the London Geochronology Centre for access to their analytical facilities,  
502 welcome and assistance. We are grateful to Kerry Gallagher for the advice on the thermal modelling,  
503 and to Mark Wildman for the discussions. Finally, we thank the two reviewers for their constructive  
504 suggestions that have led to improvements in the final version of the manuscript.

505

506 **References**

507

508 Almeida, F. F. M. 1991. O alinhamento magmatico de Cabo Frio, 2°. Simpósio de Geologia  
509 do Sudeste, São Paulo, p. 423–428.

510

511 Almeida, F.F.M.; Carneiro, C.D.R.; Mizusaki, A.M.P. 1996. Correlação do magmatismo das Bacias da  
512 Margem Continental Brasileira com o das áreas emersas adjacentes. *Revista Brasileira de*  
513 *Geociências*. v. 23 (3), p. 125–138.

514

515 Aslanian, D.; Moulin, M.; Olivet, J. L.; Unternehr, P.; Matias, L.; Bache, F.; Rabineau, M.; Nouzé, H.;  
516 Klingelhoefer, F.; Contrucci, I.; Labails, C. 2009. Brazilian and African passive margins of the  
517 Central Segment of the South Atlantic Ocean: Kinematic constraints. *Tectonophysics*. v. 468, p.  
518 98-112.

519

520 Assine, M. L.; Corrêa, F. S.; Chang, H. K. 2008. Migração de depocentros na Bacia de Santos:  
521 importância na exploração de hidrocarbonetos. *Revista Brasileira de Geociências*. v. 38(2), p.  
522 111-127.

523

524 Ault, A. K.; Flowers, R. 2012. Is apatite U–Th zonation information necessary for accurate  
525 interpretation of apatite (U–Th)/He thermochronometry data? *Geochimica et Cosmochimica*  
526 *Acta*. v. 79, p. 60-78.

527

528 Ault, A. K.; Flowers, R. M.; Bowring, S. A. 2009. Phanerozoic burial and unroofing history of the  
529 western Slave craton and Wopmay orogen from apatite (U–Th)/He thermochronometry. *Earth*  
530 *and Planetary Science Letters*. v. 284(1-2), p. 1–11.

531

532 Ault, A. K.; Gautheron, C.; King, G.E. 2019. Innovations in (U–Th)/He, fission track, and trapped  
533 charge thermochronometry with applications to earthquakes, weathering, surface-mantle  
534 connections, and the growth and decay of mountains. *Tectonics*, v.38, p. 3705-3739.

535

536 Beglinger, S. E.; Doust, H.; Cloetingh, S. 2012. Relating petroleum system and play development to  
537 basin evolution: Brazilian South Atlantic margin. *Petroleum Geoscience*. v. 18, p. 315 –336.

538

539 Blenkinsop, T.; Moore, A. 2013. Tectonic geomorphology of passive margins and continental  
540 hinterlands. In: Owen, L.A., Shroder, J.F. (Eds), *Treatise on Geomorphology 5*. Academic  
541 Press, San Diego, p. 71-92.

542

543 Brito Neves, B. B.; Cordani, U. G. 1991. Tectonic evolution of South America during the Late  
544 Proterozoic. *Precambrian Research*. v. 53, p. 23-40.  
545

546 Brito Neves, B. B.; Fuck, R. A.; Pimentel, M M. 2014. The Brasiliano collage in South America: a  
547 review. *Brazilian Journal of Geology*. v.44(3), p. 493-518.  
548

549 Brown, R. W.; Rust, D. J.; Summerfield, M. A.; Gleadow, A. J.; De Wit, M. C. 1990. An Early  
550 Cretaceous phase of accelerated erosion on the south-western margin of Africa: Evidence from  
551 apatite fission track analysis and the offshore sedimentary record. *International Journal of*  
552 *Radiation Applications and Instrumentation. Part D. Nuclear Tracks and Radiation*  
553 *Measurements*. v. 17(3), p. 339-350.  
554

555 Brown, R.W.; Summerfield, M.A.; Gleadow, A.J.W. 2002. Denudational history along transect across  
556 the Drakensberg Escarpment of southern Africa derived from apatite fission track  
557 thermochronology. *Journal of Geophysical Research*. v. 107. p. 23-50.  
558

559 Brown, R. W.; Beucher, R.; Roper, S.; Persano, C.; Stuart, F.; Fitzgerald, P. 2013. Natural age  
560 dispersion arising from the analysis of broken crystals. Part I: Theoretical basis and implications  
561 for the apatite (U–Th)/He thermochronometer. *Geochimica et Cosmochimica Acta*. v. 122, p.  
562 478-497.  
563

564 Brune, S.; Williams, S. E.; Müller, R. D. 2018. Oblique rifting: the rule, not the exception. *Solid*  
565 *Earth*. v. 9, p. 1187-1206.  
566

567 Buiter, S. J. H.; Torsvik, T. H. 2014. A review of Wilson Cycle plate margins: A role for mantle  
568 plumes in continental break-up along sutures? *Gondwana Research*. v. 26(2), p. 627-653.  
569

570 Chang, H. K.; Kowsmann, R. O.; Figueiredo, A. M. F.; Bender, A. A. 1992. Tectonics and  
571 stratigraphy of the East Brazil Rift system: an overview. *Tectonophysics*. v. 213. p. 97-138.  
572

573 Cainelli, C.; Mohriak, W. U. 1999. Some remarks on the evolution of sedimentary basins along the  
574 eastern Brazilian continental margin. *Episodes*. v. 22(3), p. 206-216.  
575

576 Cobbold, P. R.; Meisling, K. E.; Mount, V. S. 2001. Reactivation of an obliquely rifted margin,  
577 Campos and Santos Basins, Southeastern Brazil. *AAPG Bulletin*. v. 85, p. 1925-1944.  
578

579 Cogné, N.; Gallagher, K.; Cobbold, P. R. 2011. Post-rift reactivation of the onshore margin of  
580 southeast Brazil: Evidence from apatite (U–Th)/He and fission-track data. *Earth and Planetary*  
581 *Science Letters*. v. 309, Issues 1–2. p. 118-130.  
582

583 Cogné, N., Gallagher, K., Cobbold, P.R., Riccomini, C., Gautheron, C., 2012. Post-breakup tectonics  
584 in southeast Brazil from thermochronological data and combined inverse forward thermal  
585 history modeling. *Journal of Geophysical Research*. v. 117, B11413.  
586

587 Cogné, N., Cobbold, P. R., Riccomini, C. 2013. Tectonic setting of the Taubaté Basin (Southeastern  
588 Brazil): Insights from regional seismic profiles and outcrop data. *Journal of South American*  
589 *Earth Sciences*. v. 42, p. 194-204.  
590

591 Contreras, J.; Zühlke, R.; Bowman, S.; Bechstädt, T. 2010. Seismic stratigraphy and subsidence  
592 analysis of the southern Brazilian margin (Campos, Santos and Pelotas basins). *Marine and*  
593 *Petroleum Geology*. v. 27, p. 195-216.  
594

595 CPRM, 2009a. Mapa geológico. Folha Baía de Guanabara. Rio de Janeiro, RJ. SF23-Z-B-IV. Scale:  
596 1:100,000.  
597

598 CPRM, 2009b. Mapa geológico. Folha de Três Rios. Rio de Janeiro, RJ. SF23-Z-B-I. Scale:  
599 1:100,000.  
600

601 Donelick, R. A.; O'Sullivan, P. B.; Ketcham, R. A. 2005. Apatite fission-track analysis. *Reviews*  
602 *Mineralogy and Geochemistry*. v 58 (1), p. 49–94.  
603

604 Ebert, H. D.; Hasui, Y. 1998. Transpressional tectonics and strain partitioning during oblique collision  
605 between three plates in the Precambrian of south-east Brazil. In: Holdsworth, R. E.; Strachan,  
606 R. A.; Dewey, J. E (Eds.). *Continental Transpressional and Transtensional Tectonics*.  
607 Geological Society, London, Special Publications, v. 135, p. 231-252.  
608

609 Engelmann de Oliveira, C. H. E.; Jelinek, A. R.; Chemale Jr., F.; Cupertino, J. A. 2016.  
610 Thermotectonic history of the southeastern Brazilian margin: evidence from apatite fission track  
611 data of the offshore Santos Basin and continental basement. *Tectonophysics*. v. 685, p. 21-34.  
612

613 ESRI. 2016. ArcGIS Desktop: Release 10.5. Redlands, CA: Environmental Systems Research  
614 Institute.  
615

616 Farley, K. A. 2000. Helium diffusion from apatite: general behaviour as illustrated by Durango  
617 fluorapatite. *Journal of Geophysical Research*. v. 105, p. 2903-2914.  
618

619 Farley, K. A. 2002. (U-Th)/He dating: Techniques, calibrations, and applications. *Reviews in*  
620 *Mineralogy and Geochemistry*. v. 47(1), p. 819-844.  
621

622 Farley, K. A.; Wolf, R. A.; Silver, L. T. 1996. The effects of long alpha-stopping distances on (U-  
623 Th)/He ages. *Geochimica et Cosmochimica Acta*, v. 60(21), p. 4223–4229.  
624

625 Ferrari, A. L. 2001. *Evolução tectônica do Gráben da Guanabara*. PhD Thesis, University of São  
626 Paulo.  
627

628 Fitzgerald, P. G.; Baldwin, S. L.; Webb, L. E.; O'sullivan, P. B. 2006. Interpretation of (U–Th)/He  
629 single grain ages from slowly cooled crustal terranes: a case study from the Transantarctic  
630 Mountains of southern Victoria Land. *Chemical Geology*. v. 225(1), p. 91-120.  
631

632 Flowers, R. M.; Ketcham, R. A.; Shuster, D. L.; Farley, K. A. 2009. Apatite (U–Th)/He  
633 thermochronometry using a radiation damage accumulation and annealing model. *Geochimica*  
634 *et Cosmochimica Acta*. v. 73(8), p. 2347-2365.  
635

636 Flowers, R. M.; Kelley, S. A. 2011. Interpreting data dispersion and “inverted” dates in apatite  
637 (U–Th)/He and fission-track datasets: An example from the US midcontinent. *Geochimica et*  
638 *Cosmochimica Acta*. v. 75, p. 5169-5186.  
639

640 Franco-Magalhaes, A. O. B.; Hackspacher, P. C.; Glasmacher, U. A.; Saad, A. R. 2010. Rift to post-  
641 rift evolution of a “passive” continental margin: the Ponta Grossa Arch, SE Brazil. *International*  
642 *Journal of Earth Sciences*. v. 99, p. 1599-1613.  
643

644 Franco-Magalhaes, A. O. B.; Cuglieri, M. A. A.; Hackspacher, P. C.; Saad, A. R. 2014. Long-term  
645 landscape evolution and post-rift reactivation in the southeastern Brazilian passive continental  
646 margin: Taubaté basin. *International Journal of Earth Sciences*. v. 103, p. 441-453.  
647

648 Galbraith, R. F. 1992. Statistical models for mixed ages. *International Workshop on Fission Track*  
649 *Thermochronology*. Philadelphia.  
650

651 Gallagher, K. 1995. Evolving temperature histories from apatite fission-track data. *Earth and*  
652 *Planetary Science Letters*. v. 136, p. 421–435.

653  
654 Gallagher, K. 2012. Transdimensional inverse thermal history modelling for quantitative  
655 thermochronology. *Journal of Physical Research*. v. 117, p. 1-16.  
656  
657 Gallagher, K.; Brown., R. 1997. The onshore record of passive margin evolution. *Journal of the*  
658 *Geological Society*. v. 154(3), p. 451-457.  
659  
660 Gallagher, K.; Hawkesworth, C. H.; Mantovani, M. S. M. 1994. The denudation history of the onshore  
661 continental margin of the SE Brazil inferred from apatite fission track data. *Journal of*  
662 *Geophysical Research*. v. 99, n. B9. p. 18,117 -18,145.  
663  
664 Gastil, R.G.; DeLisle, M.; Morgan, J. 1967. Some effects of progressive metamorphism on zircons.  
665 *Geological Society of America Bulletin* 78, 879-906.  
666  
667 Gautheron, C.; Tassan-Got, L.; Barbarand, J.; Pagel, M. 2009. Effect of alpha-damage annealing on  
668 apatite (U-Th)/He thermochronology. *Chemical Geology*, 266(3-4), 157–170.  
669  
670 Gautheron, C.; Barbarand, J.; Ketcham, R. A.; Tassan-Got, L.; van der Beek, P. A.; Pagel, M., et al.  
671 2013. Chemical influence on  $\alpha$ -recoil damage annealing in apatite: Implications for (U-Th)/He  
672 dating. *Chemical Geology*, 351, 257–267.  
673  
674 Green, P.F. 1986. On the thermo-tectonic evolution of northern England; evidence from fission track  
675 analysis. *Geological Magazine* 123, 493–506.  
676  
677 Green, P.; Duddy, I. 2018. Apatite (U-Th-Sm)/He thermochronology on the wrong side of the tracks.  
678 *Chemical Geology*. v. 488, p. 21-33.  
679  
680 Geraldès, M. C.; Motoki, A.; Costa, A.; Mota, C. E.; Mohriak, W. U. 2013. Geochronology (Ar/Ar  
681 and K–Ar) of the South Atlantic post-break-up magmatism. In: Mohriak, W. U.; Danforth, A.;  
682 Post, P. J.; Brown, D. E.; Tari, G. C.; Nemčok, M; Sinha, S. T. (Eds.) *Conjugate Divergent*  
683 *Margins*. Geological Society, London, Special Publications. v. 369, p. 41–74.  
684  
685 Gilchrist, A.; Summerfield, M. A. 1990. Differential denudation and flexural isostasy in formation of  
686 rifted-margin upwarps, *Nature*. v. 346. p. 739-742.  
687 Gleadow. A. J. W. 1981. Fission-track dating methods: what are the real alternatives? *Nuclear Tracks*.  
688 v. 5, p. 3-14.  
689



690 Gleadow, A. J. W.; Duddy, I. R.; Green, P. F.; Lovering, J. F. 1986. Confined fission track lengths in  
691 apatite: a diagnostic tool for thermal history analysis. *Contributions to Mineralogy and*  
692 *Petrology*. v. 94(4), p. 405-415.  
693

694 Hackspacher, P. C.; Ribeiro, L. F. B.; Fetter, A. H.; Hadler Neto, J. C.; Tello Sáenz, C. E.; Dantas, E.  
695 L. 2004. Consolidation and break-up of the South American Platform in southeastern Brazil:  
696 tectonothermal and denudation histories. *Gondwana Research*. v. 7(1). p. 91-101.  
697

698 Hackspacher, P. C.; Godoy, D. F.; Ribeiro, L. F. B.; Hadler, J. C.; Franco, A.O.B. 2007. Modelagem  
699 térmica e geomorfologia da borda sul do Cráton do São Francisco: Termocronologia por traços  
700 de fissão em apatita. *Revista Brasileira de Geociências*. v. 37(4). p. 76-86.  
701

702 Hamza, V. M.; Cardoso, R. A.; Gomes, A. J. L. 2005a. Gradiente e fluxo geotérmico na região  
703 sudeste: indícios de calor residual do magmatismo alcalino e implicações para maturação  
704 térmica de sedimentos na plataforma continental, *Anais do III Simpósio de Vulcanismo e*  
705 *Ambientes Associados, Cabo Frio, Rio de Janeiro*, 319–324.  
706

707 Hamza, V.M.; Dias, F.J.S.; Gomes, A.J.L.; Terceros, Z.G.D. 2005b. Numerical and functional  
708 representations of regional heat flow in South America. *Phys. Earth Planet. Inter.* 152, 223-256.  
709

710 Heilbron, M.; Valeriano, C. M.; Tassinari, C. C. G.; Almeida, J.; Tupinambá, M.; Siga Jr., O.; Trouw,  
711 R. 2008. Correlation of Neoproterozoic terranes between the Ribeira Belt, SE Brazil and its  
712 African counterpart: comparative tectonic evolution and open questions. In: Pankhurst, R. J.;  
713 Trouw, R. A. J.; Brito Neves, B. B.; De Wit, M. J. (Eds.). *West Gondwana: Pre-Cenozoic*  
714 *Correlations Across the South Atlantic Region*. London, The Geological Society of London  
715 *Special Publications*. v. 294, p. 211–237.  
716

717 Heilbron, M.; Silva, L. G. E.; Almeida, J. C. H.; Tupinambá, M.; Peixoto, C.; Valeriano, C. M.;  
718 Lobato, M.; Rodrigues, S.W. O.; Ragatky, C. D.; Silva, M. A.; Monteiro, T.; Freitas, N. C.;  
719 Miguens, D.; Girão, R. 2020. Proterozoic to Ordovician geology and tectonic evolution of Rio  
720 de Janeiro State, SE-Brazil: insights on the central Ribeira Orogen from the new 1:400,000  
721 scale geologic map. *Brazilian Journal of Geology*. v. 50(2). p. 1-25.  
722

723 Heine, C.; Zoethout, J.; Müller, R. D. 2013. Kinematics of the South Atlantic rift. *Solid Earth*. v. 4. p.  
724 215-253.  
725

726 Hiruma, S. T.; Riccomini, C.; Modenesi-Gauttieri, M. C.; Hackspacher, P. C.; Hadler Neto, J. C.;  
727 Franco-Magalhães, A. O. B. 2010. Denudation history of the Bocaina Plateau, Serra do Mar,  
728 southeastern Brazil: Relationships to Gondwana breakup and passive margin development.  
729 *Gondwana Research*. v. 18(4), p. 674-687.  
730

731 Hourigan J. K., Reiners P. W. and Brandon M. T. 2005. U–Th zonation-dependent a-ejection in (U–  
732 Th)/He chronometry. *Geochimica et Cosmochimica Acta*. v. 69, p. 3349–3365.  
733

734 Hueck, M.; Dunkl, I.; Oriolo, S.; Wemmer, K.; Basei, M. A. S.; Siegesmund, S. 2019. Comparing  
735 contiguous high- and low-elevation continental margins: New (U-Th)/He constraints from  
736 South Brazil and an integration of the thermochronological record of the southeastern passive  
737 margin of South America. *Tectonophysics*. v. 770, 228222.  
738

739 Hurford, A. J. 1990. Standardization of fission track dating calibration: Recommendation by the  
740 Fission Track Working Group of the I.U.G.S. Subcommittee on Geochronology. *Chemical*  
741 *Geology*. v. 80, p. 171-178.  
742

743 Hurford, A. J.; Green, P. F. 1982. A user's guide to fission track dating calibration. *Earth and*  
744 *Planetary Science Letters*. v. 59, p. 343-354.  
745

746 Janasi, V. A.; Freitas, V. A.; Heaman, L. H. 2011. The onset of flood basalt volcanism, Northern  
747 Paraná Basin, Brazil: A precise U–Pb baddeleyite/zircon age for a Chapecó-type dacite. *Earth*  
748 *and Planetary Science Letters*. v. 302, p. 147-153.  
749

750 Japsen, P.; Chalmers, J. A.; Green, P. F.; Bonow, J. M. 2012. Elevated, passive continental margins:  
751 Not rift shoulders, but expressions of episodic, post-rift burial and exhumation. *Global and*  
752 *Planetary Change*. v. 90–91. p. 73-86.  
753

754 Jelinek, A. R.; Chemale, Jr., F.; van der Beek, P. A.; Guadagnin, F.; Cupertino, J. A. 2014.  
755 Denudation history and landscape evolution of the northern East-Brazilian continental margin  
756 from apatite fission-track thermochronology. *Journal of South American Earth Sciences*. v. 54,  
757 p. 158-181.  
758

759 Karl, M.; Glasmacher, U. A.; Kollenz, S.; Franco-Magalhães, A. O. B.; Stockli, D. F.; Hackspacher,  
760 P. C. 2013. Evolution of the South Atlantic passive continental margin in southern Brazil  
761 derived from zircon and apatite (U-Th-Sm)/He and fission-track data. *Tectonophysics*. v. 604,  
762 p. 224-244.

763  
764 Karner, G. D.; Driscoll, N. W. 1999. Tectonic and stratigraphic development of the West African and  
765 eastern Brazilian Margins: insights from quantitative basin modelling. In: Cameron, N. R.;  
766 Bate, R. H.; Clure, V. S. (Eds.). *The Oil and Gas Habitats of the South Atlantic*. London, The  
767 Geological Society of London Special Publications. v. 153, p. 11-40.  
768  
769 Ketcham, R. A.; Carter, A.; Donelick, R. A.; Barbarand, J.; Hurford, A. J. 2007. Improved modelling  
770 of fission-track annealing in apatite. *American Mineralogist*. v 92(5-6), p. 799-810.  
771  
772 Krob, F. C.; Glasmacher, U. A.; Karl, M.; Perner, M.; Hackspacher, P. C.; Stockli, D. F. 2019. Multi-  
773 chronometer thermochronological modelling of the Late Neoproterozoic to recent t-T-evolution  
774 of the SE coastal region of Brazil. *Journal of South American Earth Sciences*. v. 92, P. 77-94.  
775  
776 Lima Gomes, A. J.; Hamza, V. M. 2005. Geothermal gradient and heat flow in the state of Rio de  
777 Janeiro. *Revista Brasileira de Geofísica*. v. 23(4), p. 325-347.  
778  
779 Lippolt, H. J.; Leitz, M.; Wernicke, R. S.; Hagedorn, B. 1994. (Uranium+thorium)/helium dating of  
780 apatite: experience with samples from different geochemical environments. *Chemical Geology;*  
781 *Isotope Geoscience*. v. 112, p. 179–191.  
782  
783 Macdonald, D.; Gomez-Perez, I.; Franzese, J.; Spalletti, L.; Lawyer, L.; Gahagan, L.; Dalziel, I.;  
784 Thomas, C.; Trewin, N.; Hole, M.; Paton, D. 2003. Mesozoic break-up of SW Gondwana:  
785 implications for regional hydrocarbon potential of the southern South Atlantic. *Marine and*  
786 *Petroleum Geology*. v. 20, Issues 3–4, p. 287-308.  
787  
788 Mascle, J., 1976. Atlantic-type continental margins: distinction of two basic structural types. *Anais da*  
789 *Academia Brasileira de Ciências*. v. 48. p. 191-197.  
790  
791 McGregor, E. D.; Nielsen, S. B.; Stephenson, R. A.; Petersen, K. D.; Macdonald, D. I. M. 2013. Long-  
792 term exhumation of a Palaeoproterozoic orogen and the role of pre-existing heterogeneous  
793 thermal crustal properties: a fission-track study of SE Baffin Island. *Journal of the Geological*  
794 *Society, London*. v. 170, p. 877-891.  
795  
796 Meesters, A. G. C. A.; Dunai, T. J. 2002a. Solving the production–diffusion equation for finite  
797 diffusion domains of various shapes: Part I. Implications for low-temperature (U–Th)/He  
798 thermochronology. *Chemical Geology*. v. 186(3), p. 333-344.  
799

800 Meesters, A. G. C. A.; Dunai, T. J. 2002b. Solving the production–diffusion equation for finite  
801 diffusion domains of various shapes: Part II. Application to cases with  $\alpha$ -ejection and  
802 nonhomogeneous distribution of the source. *Chemical Geology*. v. 186(3), p. 347-363.  
803

804 Meisling, K. E.; Cobbold, P. R.; Mount, V. S. 2001. Segmentation of an obliquely rifted margin,  
805 Campos and Santos basins, southeastern Brazil. *AAPG Bulletin*. v. 85(11), p. 1903-1924.  
806

807 Milani, E. J.; Brandão, A. S. L.; Zalán, P. V.; Gambia, L. A. P. 2001. Petróleo na margem continental  
808 brasileira: geologia, exploração, resultados e perspectivas. *Brazilian Journal of Geophysics*. v.  
809 18, p. 352-396.  
810

811 Modica, C. J.; Brush, E. R. 2004. Postrift sequence stratigraphy, paleogeography, and fill history of  
812 the deep-water Santos Basin, offshore southeast Brazil. *AAPG Bulletin*. v. 88, p. 923–945.  
813

814 Mohriak, W. U.; Hobbs, R.; Dewey, J. F. 1990. Basin-forming processes and the deep structure of the  
815 Campos Basin, offshore Brazil. *Marine and Petroleum Geology*. v. 7(2), p. 101-122.  
816

817 Murray, K. E.; Orme, D. A. Reiners, P. W. 2014. Effects of U–Th-rich grain boundary phases on  
818 apatite helium ages. *Chemical Geology*. v. 390, p. 135-151.  
819

820 Nielsen, S. B.; Gallagher, K.; Leighton, C.; Balling, N.; Svenningsen, L.; Jacobsen, B. H.; Thomsen,  
821 E.; Nielsen, O. B.; Heilmann-Clausen, C.; Egholm, D. L.; Summerfield, M. A.; Clausen, O. R.;  
822 Piotrowski, J. A.; Thorsen, M. R.; Huuse, M.; Abrahamsen, N.; King, C.; Lykke-Andersen, H.  
823 2009. The evolution of western Scandinavian topography: A review of Neogene uplift versus  
824 the ICE (isostasy–climate–erosion) hypothesis. *Journal of Geodynamics*. v. 47, (2-3), p. 72-95.  
825

826 O’Sullivan, P. B; Mitchell, M. M.; O’Sullivan, A. J.; Kohn, B. P.; Gleadow, A. 2000. Thermotectonic  
827 history of the Bassian Rise, Australia: Implications for the breakup of eastern Gondwana along  
828 Australia’s southeastern margins, *Earth Planet. Sci. Lett.*, 182, 31–47.  
829

830 Pichel, L. M.; Jackson, C. A.; Peel, F.; Dooley, T. P. 2019. Base-Salt Relief Controls on Salt-tectonic  
831 Structural Style, São Paulo Plateau, Santos Basin, Brazil. *Basin*  
832 *Research*.doi:10.1111/bre.12375  
833

834 Raab, M. J.; Brown, R. W.; Gallagher, K.; Carter, A.; Weber, K. 2002. Late Cretaceous reactivation of  
835 major crustal shear zones in northern Namibia: constraints from apatite fission track analysis.  
836 *Tectonophysics*. v. 349(1), p. 75-92.

837  
838 Recanati, A.; Gautheron, C.; Barbarand, J.; Missenard, Y.; Rinna-Jamme, R.; Tassan-Got, L.; et al.  
839 2017. Helium trapping in apatite damage: Insights from (U-Th-Sm)/He dating of different  
840 granitoid lithologies. *Chemical Geology*, 470, 116–131.  
841  
842 Reiners, P. W.; Farley, K. A. 2001. Influence of crystal size on apatite (U–Th)/He thermochronology:  
843 an example from the Bighorn Mountains, Wyoming. *Earth and Planetary Science Letters*. v.  
844 188(3–4), p. 413-420.  
845  
846 Riccomini, C.; Sant’Anna, L.G.; Ferrari, A.L. 2004. Evolução geológica do Rift Continental do  
847 Sudeste do Brasil. In: Mantesso-Neto, V., Bartorelli, A., Carneiro, C.D.R., Brito-Neves, B.B.  
848 (Eds.), *Geologia do Continente Sul-Americano: Evolução da Obra de Fernando Flávio Marques*  
849 *de Almeida*. Edições Beca, São Paulo. p. 383–405.  
850  
851 Riccomini, C.; Velázquez, V.F.; Gomes, C.B. 2005. Tectonic controls of the Mesozoic and Cenozoic  
852 alkaline magmatism in central-southeastern Brazilian Platform. In: Gomes, C.B., Comin-  
853 Chiamonti, P. (Eds.), *Mesozoic to Cenozoic Alkaline Magmatism in the Brazilian Platform*.  
854 EDUSP-FAPESP, São Paulo. p. 31–55.  
855  
856 Sacek, V.; Braun, J.; van der Beek, P. 2012. The influence of rifting on escarpment migration on high  
857 elevation continental margins. *Journal of Geophysical Research*. v. 117, B04407.  
858  
859 Santos, R. P. 1994. Datation K/Ar e Rb/Sr d’argilles de mineralisation et de diagenèse le long de côte  
860 de l’Amerique du Sud. Implications geodynamiques. PhD Thesis, University of Grenoble I.  
861  
862 Stanton, N.; Schmitt, R.; Galdeano, A.; Maia, M.; Mane, M. 2010. Crustal structure of the  
863 southeastern Brazilian margin, Campos Basin, from aeromagnetic data: New kinematic  
864 constraints. *Tectonophysics*. v. 490, p. 15-27.  
865  
866 Schmitt, R. S.; Throuw, R. A. J.; Van Schmus, W. R.; Passchier, C. W. 2008. Cambrian orogeny in  
867 the Ribeira Belt (SE Brazil) and correlations within West Gondwana: ties that bind underwater.  
868 In: Pankhurst, R. J.; Trouw, R. A. J.; Brito Neves, B. B.; de Wit, M. J. (Eds.). *West Gondwana:*  
869 *Pre-Cenozoic correlations across the South Atlantic Region*. London, The Geological Society of  
870 London Special Publications. v. 294. p. 279-296.  
871  
872 Schmitt, R. S.; Trouw, R.; Van Schmus, W. R.; Armstrong, R.; Stanton, N. S. G. 2016. The tectonic  
873 significance of the Cabo Frio Tectonic Domain in the SE Brazilian margin: a Paleoproterozoic

874 through Cretaceous saga of a reworked continental margin. *Brazilian Journal of Geology*. v.  
875 46(1), p. 37-66.

876

877 Shuster, D. L.; Flowers, R. M.; Farley, K. A. 2006. The influence of natural radiation damage on  
878 helium diffusion kinetics in apatite. *Earth and Planetary Science Letters*. v. 249(3), p. 148-161.  
879

880 Spiegel C.; Kohn B. P.; Belton D.; Brener Z.; Gleadow A. J. W. 2009. Apatite (U–Th–Sm)/He  
881 thermochronology of rapidly cooled samples: the effect of He implantation. *Earth and Planetary  
882 Science Letters*. v. 385, p. 105–119.  
883

884 Stica, J. M.; Zalán, P. V.; Ferrari, A. L. 2014. The evolution of rifting on the volcanic margin of the  
885 Pelotas Basin and the contextualization of the Paraná Etendeka LIP in the separation of  
886 Gondwana in the South Atlantic. *Marine and Petroleum Geology*. v. 50, p. 1-21.  
887

888 Stockli, D. F.; Farley, K. A.; Dumitru, T. A. 2000. Calibration of the apatite (U–Th)/He  
889 thermochronometer on an exhumed fault block, White Mountains, California. *Geology*. v. 28, p.  
890 983–986.  
891

892 Tello S., C. A.; Hackspacher, P. C.; Hadler Neto, J.C.; Iunes, P. J.; Guedes, S.; Paulo, S. R.; Ribeiro,  
893 L. F. B. 2003. Recognition of Cretaceous, Paleocene and Neogene tectonic reactivation, through  
894 apatite fission-track analysis, in Precambrian areas of the Southeast Brazil: association with the  
895 South Atlantic Ocean opening. *Journal of South American Earth Sciences*. v. 15, p. 137–142.  
896

897 Tello S., C. A.; Hadler Neto, J. C.; Iunes, P. J.; Guedes, S.; Hackspacher, P. C.; Ribeiro L. F. B.;  
898 Paulo, S. R.; Osório, A. M. A. 2005. Thermochronology of the South American Platform in the  
899 state of São Paulo, Brazil, through apatite fission tracks. *Radiation Measurements*. v. 39, p.  
900 635–640.  
901

902 Thiede, D. S.; Vasconcelos, P. M. 2010. Paraná flood basalts: Rapid extrusion hypothesis confirmed  
903 by new  $^{40}\text{Ar}/^{39}\text{Ar}$  results. *Geology*. v. 38(8), p. 747-750.  
904

905 Thomaz Filho, A.; Mizusaki, A. M. P.; Antonioli, L. 2008. Magmatismo nas bacias sedimentares  
906 brasileiras e sua influência na geologia do petróleo. *Revista Brasileira de Geociências*. v. 38(2),  
907 p. 128-137.  
908

909 Thompson, R. N.; Gibson, S. A.; Mitchell, J. G.; Dickin, A.P.; Leonardos, O. H.; Brod, J. A.;  
910 Greenwood, J. C. 1998. Migrating Cretaceous-Eocene magmatism in the Serra do Mar Alkaline

911 Province, SE Brazil: Melts from the deflected Trindade Mantle Plume? *Journal of Petrology*. v.  
912 39, p. 1493-1526.

913

914 Tommasi, A.; Vauchez, A. 2001. Continental rifting parallel to ancient collisional belts: an  
915 effect of the mechanical anisotropy of the lithospheric mantle. *Earth and Planetary Science Letters*. v.  
916 185, p. 199-210.

917

918 Trouw, R. A. J.; Heilbron, M.; Ribeiro, A.; Paciullo, F. V. P.; Valeriano, C. M.; Almeida, J. C. H.;  
919 Tupinambá, M.; Andreis, R. R. 2000. The central segment of the Ribeira Belt. In: Cordani, U.  
920 G.; Milani, E. J.; Thomaz Filho, A.; Campos, D. A. (Eds.). *Tectonic evolution of South*  
921 *America*. 31st International Geological Congress. Rio de Janeiro. p. 287-310.

922

923 Vieira, B. C.; Gramani, M. F. 2015. Serra do Mar: the most “tormented” relief in Brazil. In: Vieira, B.  
924 C.; Salgado, A. A. R.; Santos, L. J. C. (Eds.). *Landscape and landforms of Brazil*. Springer. p.  
925 285-298.

926

927 Wagner, G. A.; Gleadow, A. J. W.; Fitzgerald, P. G. 1989. The significance of the partial annealing  
928 zone in apatite fission-track analysis: Projected track length measurements and uplift  
929 chronology of the Transantarctic Mountains. *Chemical Geology (Isotope Geoscience Section)*.  
930 v. 79, p. 295–305.

931

932 Wildman, M.; Brown, R.; Watkins, R. Carter, A.; Gleadow, A.; Summerfield, M. 2015. Post break-up  
933 tectonic inversion across the southwestern cape of South Africa: New insights from apatite and  
934 zircon fission track thermochronometry. *Tectonophysics*. v. 654, p. 30-55.

935

936 Wildman, M.; Cogné, N.; Beucher, R. 2019. Fission-Track Thermochronology Applied to the  
937 Evolution of Passive Continental Margins. In: Malusà, M. G.; Fitzgerald P. G. (Eds.). *Fission-*  
938 *Track Thermochronology and its Application to Geology*. Springer Textbooks in Earth  
939 *Sciences, Geography and Environment*. p. 351-371.

940

941 Zalán, P. V.; Oliveira, J. A. B. 2005. Origem e evolução estrutural do Sistema de Riftes Cenozóicos  
942 do Sudeste do Brasil. *Boletim de Geociências da Petrobras*. v. 13. p. 269-300.

943

944 **Table 1.** Summary of apatite fission track data.

Sample	Lat	Long	Elev. (m)	No of crystals	Dosimeter		Spontaneous		Induced		Age dispersion		Central Age (Ma)	±1σ (Ma)	Mean Cl wt %	MTL (μm)	S.D. (μm)	n	Mean Dpar (μm)
					ρ <sub>s</sub>	N <sub>s</sub>	ρ <sub>s</sub>	N <sub>s</sub>	ρ <sub>i</sub>	N <sub>i</sub>	Pχ <sup>2</sup>	RE%							
JG-1	-22.94	-43.16	0	20	1.687	4676	1.169	1369	4.689	5542	30.7	5.0	70.1	2.5	0.01	13.10	1.4	75	1.5
JG-2	-22.94	-43.15	16	20	1.687	4676	0.227	205	1.172	1075	99.1	0.0	54.1	4.2	0.01	-	-	-	-
JG-4	-22.56	-43.26	287	20	1.687	4676	0.384	185	1.593	781	94.8	0.0	67.2	5.6	0.002	-	-	-	-
RJ-5	-22.55	-43.22	612	20	1.819	5042	0.481	324	1.574	1126	31.8	3.4	87.9	5.7	-	12.83	1.6	49	2.6
RJ-6	-22.54	-43.22	768	20	1.819	5042	0.596	382	2.087	1345	25.9	4.3	86.9	5.3	-	-	-	-	2.3
RJ-7	-22.53	-43.22	812	20	1.819	5042	0.859	6.5	3.112	2223	67.9	0.4	83.1	4.0	-	12.94	1.6	90	2.4
JG-12	-22.51	-43.23	774	20	1.687	4676	0.765	456	2.98	1791	79.9	0.0	72.2	3.9	0.000	13.08	1.2	100	2.1
JG-14	-22.53	-43.24	444	20	1.687	4676	0.887	514	3.431	2031	15.16	9.4	72.4	4.1	0.001	13.59	1.5	105	2.2
RJ-15	-22.54	-43.25	318	20	1.819	5042	0.541	379	2.486	1691	68.5	4.0	68.5	4.1	-	12.34	1.7	19	1.8
JG-16	-22.55	-43.27	178	20	1.687	4676	1.097	742	4.358	3014	31.05	8.5	70.3	3.4	0.06	12.57	1.5	102	1.9
JG-17	-22.28	-43.13	663	19	1.687	4676	1.086	567	3.76	1955	84.2	0.0	82.2	4.1	0.017	13.55	1.6	83	3.5
JG-18	-22.30	-43.13	706	17	1.687	4676	1.856	992	6.887	3611	33.5	1.2	77.8	3.0	0.01	13.19	1.4	90	1.6
JG-20	-22.40	-43.10	740	30	1.687	4676	0.207	251	0.666	828	94.2	0.2	85.9	6.3	0.008	-	-	-	1.7
JG-22	-22.41	-43.06	1155	22	1.687	4676	0.314	214	1.108	837	5.2	24.3	75.0	7.1	0.005	13.71	1.3	3	1.6
JG-23A	-22.41	-43.05	1216	21	1.687	4676	0.725	300	2.797	1198	27.7	14.9	71.3	5.3	0.002	13.89	1.1	55	1.8
RJ-24	-22.40	-43.05	1303	20	1.819	5042	0.57	337	2.111	1285	29.2	5.8	80.3	5.2	-	13.18	1.3	100	2.4
RJ-25	-22.40	-43.04	1436	20	1.819	5042	0.947	692	3.23	2390	58.4	0.4	88.4	4.0	-	12.81	1.0	100	2.4
JG-26	-22.44	-43.00	1179	20	1.687	4676	0.75	456	2.512	1543	39.4	7.1	83.7	4.8	0.0004	13.59	1.3	103	2.0
JG-27	-22.44	-42.99	1043	20	1.687	4676	0.919	511	3.073	1709	59.4	0.2	84.7	4.4	0.017	13.34	1.4	110	1.7
RJ-33	-22.40	-43.14	751	20	1.819	5042	1.073	674	3.999	2517	67.2	0.3	81.8	3.7	-	12.94	1.3	100	1.9
JG-35	-22.17	-43.17	297	20	1.687	4676	0.802	816	1.687	2727	30.8	4.9	84.8	3.7	0.044	13.33	1.3	100	1.7
RJ-36	-22.10	-43.17	291	20	1.819	5042	1.231	1017	4.046	3415	0.6	14.6	91.3	4.7	-	13.15	1.4	100	2.0
RJ-37	-22.04	-43.20	330	20	1.819	5042	1.058	1078	3.426	3462	32.3	0.4	95.0	3.6	-	12.99	1.7	70	2.3
JG-38	-22.01	-43.24	314	20	1.687	4676	0.135	232	0.56	966	94.9	0.0	68.1	5.1	0.006	-	-	-	-
J-42	-22.92	-43.12	6	20	1.762	4784	0.94	930	3.703	3681	56.2	0.8	74.8	3.0	-	13.90	1.6	77	2.5
J-43	-22.97	-43.03	4	20	1.762	4784	1.562	955	5.72	3598	19.4	4.6	78.8	3.2	-	13.83	1.4	94	3.1
J-44	-22.95	-43.02	134	20	1.762	4784	1.161	931	4.201	3425	23.3	5.2	80.5	3.3	-	13.56	1.5	109	2.5
J-45	-22.46	-43.08	1541	20	1.762	4784	0.527	685	1.588	2055	8.2	11.9	98.5	5.3	-	14.63	1.4	71	3.6
J-46	-22.43	-43.01	1513	20	1.762	4784	0.406	386	1.216	1199	6.2	18.6	96.1	7.1	-	13.90	1.6	20	2.4
J-49	-22.66	-43.11	16	20	1.762	4784	0.871	819	3.034	2832	19.1	8.0	85.5	3.9	-	13.93	1.3	103	4.1

981  
982  
983  
984 Track densities are (x10<sup>6</sup> tr cm<sup>-2</sup>); analyses by external detector method using 0.5 for the 4π/2π geometry correction factor; central age is a modal age, weighted for different precisions of individual crystals (Galbraith,  
985 1992); ρ<sub>s</sub>: measured spontaneous track density; N<sub>s</sub>: number of spontaneous tracks counted; ρ<sub>i</sub>: measured induced track density; N<sub>i</sub>: number of induced tracks counted; ρ<sub>d</sub>: track density measured in glass dosimeter;  
986 N<sub>d</sub>: number of tracks counted in determining ρ<sub>d</sub>; 1σ: standard deviation; χ<sup>2</sup>: Chi-square probability; n: number of confined tracks lengths measured; MTL: mean track length; Dpar: mean etch pit diameter of all  
987 measured etch pits; S.D.: standard deviation of track length distribution of individual track measurements; (-): not analysed. Note: AFT ages were calculated by Prof. A. Carter using ζ CN5= 338.5 calibrated by  
988 multiple analyses of IUGS apatite and zircon age standards (Hurford, 1990). Coordinate datum WGS 84.

989  
990  
991



992  
993  
994  
995  
996  
997  
998  
999  
000  
001  
002  
003  
004  
005  
006  
007  
008  
009

**Table 2.** Summary of results for Apatite U-Th/He analysis

Sample	Aliquot	<sup>4</sup> He (ncc)	Mass (mg)	U (ppm)	Th (ppm)	Sm (ppm)	Th/U ratio	L (µm)	W (µm)	R* (µm)	FT	Raw Age (Ma)	Corrected <sup>a</sup> Age (Ma)	[eU] (ppm)	Raw Age (Ma)		Corrected Age (Ma)	
															Average	SD	Average	SD
JG-01	1	5.7314	0.0199	24.8	41.8	216.2	1.69	298.3	164.0	96.4	0.83	67.5	80.3	34.6	60.2	7.3	72.9	8.2
	2	2.4255	0.0108	25.5	28.0	327.5	1.10	275.4	125.8	76.8	0.78	56.5	70.5	32.1				
	3	3.0366	0.0156	21.3	24.0	253.3	1.13	280.5	149.5	88.5	0.81	58.6	70.8	26.9				
	4	4.1763	0.0174	24.9	26.3	336.6	1.06	313.4	149.4	90.5	0.81	62.5	75.1	31.1				
	5	2.4286	0.0138	24.7	19.3	338.3	0.78	270.1	143.6	85.1	0.80	48.5	59.0	29.2				
	6	7.2922	0.0193	31.2	59.3	401.8	1.90	348.5	149.3	92.2	0.82	67.8	81.5	45.1				
JG-26	1	0.8858	0.0040	21.71	9.04	124.71	0.42	169.0	97.9	56.9	0.70	74.9	101.7	23.8	64.0	8.6	92.0	11.0
	2	0.3060	0.0023	14.29	11.13	58.50	0.78	129.2	85.1	48.0	0.65	63.4	92.6	16.9				
	3	0.6056	0.0035	19.03	29.60	208.29	1.56	201.5	83.8	52.0	0.68	53.8	76.3	26.0				
	4	0.3509	0.0019	19.64	16.66	94.50	0.85	123.1	78.6	44.7	0.62	64.2	97.2	23.6				
JG-37	1	10.3538	0.0276	29.04	50.82	38.33	1.75	338.3	181.3	107.2	0.84	74.8	87.3	41.0	68.1	5.9	81.6	5.4
	2	5.6901	0.0157	33.72	44.83	62.42	1.33	268.7	153.2	89.4	0.81	67.0	80.9	44.3				
	4	4.9315	0.0117	44.25	57.64	50.46	1.30	252.6	136.6	80.6	0.79	59.6	73.5	57.8				
	5	11.8001	0.0240	38.17	72.60	49.88	1.90	347.4	166.9	100.9	0.83	72.7	85.8	55.2				
	6	4.4998	0.0160	23.82	45.27	53.30	1.90	293.2	148.4	88.8	0.81	66.5	80.6	34.5				

010 Aliquot refers to single grain ages measured in a given sample; L is grain length; W is grain width; R\* is the spherical equivalent radius calculated using the formula  $R^* = (3(RL))/(2(R+L))$   
011 where R is the measured radius of the apatite crystal (W/2) and L is the measured length of the apatite crystal; FT is the correction factor after Farley et al. (1996), assuming homogeneous  
012 distribution U and Th; eU (effective uranium) is calculated as  $FT = [eUppm] = [Uppm] + (0.235[Thppm])$ . a: Corrected AHe age = Raw AHe age/FT.